INL/RPT-22-67941 Rev. 000

Implementation and testing of physics-based pulverization model in BISON

Technical Report

Larry K. Aagesen[1], Sudipta Biswas[1], Kyle A. Gamble[1], Wen Jiang[1], Pierre-Clément Simon[1], and Benjamin Spencer[1]

[1]Idaho National Laboratory

INL is a U.S. Department of Energy National Laboratory operated by Batelle Energy Alliance, LLC

Implementation and testing of physics-based pulverization model in BISON

Technical Report

Larry K. Aagesen[1], Sudipta Biswas[1], Kyle A. Gamble[1], Wen Jiang[1], Pierre-Clément Simon[1], and Benjamin Spencer[1]

[1]Idaho National Laboratory

June 30, 2022

Idaho National Laboratory
Computational Mechanics and Materials Department
Idaho Falls, Idaho 83415

http://www.inl.gov

Prepared for the
U.S. Department of Energy
Office of Nuclear Energy
Under U.S. Department of Energy-Idaho Operations Office
Contract DE-AC07-05ID14517

Page intentionally left blank

Abstract

This report summarizes lower length scale computational research conducted to improve the pulverization criterion for high-burnup UO_2 fuel in the BISON fuel performance code. This research was sponsored by the NEAMS program during FY22. Efforts to improve the model primarily focus on calculating the current pressure of bubbles in the high-burnup structure (HBS) region, as well as the critical bubble pressure at which pulverization occurs in the HBS. The phase-field model for predicting initial bubble pressure in the HBS was improved by implementing a more realistic model for defect production, and by coupling the phase-field model for inter-granular bubble evolution with the spatially-resolved cluster dynamics code Xolotl to simulate intra-granular fission gas evolution. An evolution equation for current bubble pressure was added to BISON, an improvement over the previous model that assumed that bubble pressure was static following HBS formation. To improve calculations of critical bubble pressure for pulverization, 3-D phase-field fracture simulations were performed, and a function for critical bubble pressure was fit—based on the simulation results—to replace the previous function, which had been determined using 2-D simulations. The impacts of these modifications to the existing pulverization assessment cases will be reported in the forthcoming engineering-scale milestone on high-burnup UO_2 pulverization. A poromechanics-based approach was used to include the effect of bubble overpressurization on the stress state of the pellet at the engineering scale, and the initial strategy for integration of the pulverization criterion with pellet-scale mechanical degradation using a smeared cracking model was developed. This report also describes the initial research that was conducted to inform a forthcoming transient fission gas release (tFGR) model in BISON. Focusing on the fission gas release caused by pulverization of the outer pellet rim, a model for the amount of fission gas release was developed as a function of fuel porosity, bubble size, and fragment size. Implementation of this model in BISON and its impact of engineering-scale predictions will also be described in the aforementioned engineering-scale milestone on high-burnup UO_2 pulverization.

Page intentionally left blank

Acknowledgments

This report was authored by a contractor of the U.S. Government under contract DE-AC07-05ID14517. Accordingly, the U.S. Government retains a non-exclusive, royalty-free license to publish or reproduce the published form of this report, or allow others to do so, for U.S. Government purposes.

This research made use of the resources of the High Performance Computing Center at Idaho National Laboratory, which is supported by the DOE Office of Nuclear Energy and the Nuclear Science User Facilities under contract no. DE-AC07-05ID14517.

Page intentionally left blank

Contents

List of Figures

5.3 Predicted f_V^{pul} values for different pore structures in fuel fragments, along with a fit using a linear regression. (a) Shows the data in 3-D. (b, c) Show the data along r_b/l_f for extreme porosity values, and along the porosity for extreme r_b/l_f values, respectively. f_V^{pul} does not significantly depend on porosity, but increases on average with r_b/l_f. Despite an appropriate fitting, the quality of the fit is equal to $R^2 = 0.79$, due to large variations in f_V^{pul} for some pore structures, especially for low porosities. 51

List of Tables

1. INTRODUCTION

To improve the economics of commercial nuclear reactors, nuclear vendors and utilities are seeking approval for the increased burnup usage of the existing nuclear fleet—something especially critical for meeting the clean energy initiative of the U.S. Government and Department of Energy. However, a key challenge faced by the nuclear industry in this regard is that regions of UO_2 fuel exposed to high burnups and low temperatures exhibit a fine-grained microstructure with large bubbles, known as a high-burnup structure (HBS) [1]. HBS has been observed in various types of nuclear fuels, including ceramics and metals [2, 3, 4]. Key characteristics of the HBS region include (1) the accumulation of dislocations, creating large dislocation networks; (2) the formation of new, defect-free subgrains; (3) the depletion of intra-granular fission gas concentrations; and (4) the development of large spherical inter-granular bubbles. HBS formation has been correlated to diminished reactor performance, leading to accelerated fission gas release, as well as fuel fragmentation and pulverization during transient and accident conditions [2]. Thus, it is paramount to understand the mechanisms of HBS formation, along with its impact on the properties and performance of nuclear fuels. Pulverization has been noted in both partially and fully recrystallized high-burnup regions. Although the reason behind this pulverization is not fully understood, it has been attributed to fine-grained structures with high-pressure bubbles. With grain subdivision, the grain boundary (GB) density in the fuel increases, weakening the fracture strength and leading to fuel fragmentation. The possibility of pulverization during a loss-of-coolant accident (LOCA) is currently a major obstacle for the nuclear industry in regard to obtaining regulatory approval for higher burnup limits. To better understand the conditions under which pulverization may occur, as well as the resulting impacts, the capability to model HBS formation and the resulting probability of pulverization is crucial. A primary effect of fuel pulverization is the sudden release of a large amount of fission gas. This large fission gas release becomes increasingly significant with increasing burnup, and may impact the ballooning and burst behavior of high-burnup fuel [5, 6].

This report details activities carried out under the NEAMS program during fiscal year (FY) 22 to improve a physics-based model of pulverization in high-burnup UO_2 (a model originally developed in FY21 [7]), and to inform development of a model for transient fission gas release (tFGR) resulting from this pulverization. The report is structured as follows. In Section 2, phase-field modeling of the HBS evolution is used to inform calculations of the initial pressure of bubbles in the HBS region. The new developments in the phase-field model are described in detail. In Section 3, 3-D phase-field fracture simulations are employed to calculate the critical pressure (i.e., the pressure at which pulverization will occur) of bubbles in the HBS region. Previous simulations for calculating this quantity were performed in 2-D. The 3-D simulations are much more expensive computationally, but also much more representative of the actual geometry and stress state surrounding the bubbles. Section 4 describes updates to the Bison model for the calculation

of the current bubble pressure. The new version of the model considers vacancy flux, which causes bubbles in the HBS region to grow and decrease in pressure. A new function for the critical pressure at which pulverization occurs is fit based on the phase-field simulations of Section 3. A poromechanics-based approach is also used to determine the effect of bubble overpressurization on the stress state of the fuel at the engineering scale. Section 5 discusses the initial development of a model for tFGR due to pulverization. As pulverization occurs, gas trapped within the bubbles escapes to the fuel rod free volume, adding to the gas already released via the normal diffusional process. The tFGR level is modeled as a function of bubble pressure, porosity, bubble size, and fuel fragment size.

2. HBS FORMATION AND BUBBLE GROWTH

2.1 Phase-field modeling strategies to incorporate a more realistic understanding of defects

Phase-field modeling has become a well-established technique for simulating the microstructural evolution of nuclear fuel, including the grain structure and fission gas bubble microstructure. A model for the evolution of the fission gas bubble microstructure in UO_2 was previously developed though the NEAMS program [8]. This model is based on a functional of the grand potential density of the system, and includes order parameters that represent the bubble phase and an arbitrary number of grains of the solid UO_2 phase. The defect species considered in this model are monovacancies on U lattice sites and Xe atoms, which are assumed to sit on U monovacancy sites.

Although the model represented a step forward in terms of making a more physically grounded representation of the fission gas bubble microstructure of nuclear fuel, several simplifications nonetheless remain in the model's treatment of defect species. The production rate of the Xe defects is based on the product of the fission rate and fission yield of Xe atoms, and is thus expected to closely match the physical production rate. However, the production rate of monovacancies is assumed to be a multiple of the fission rate. This is meant to mimic the production bias of vacancies relative to interstitials. However, the physical value of this effective vacancy source term is not well known. Previously, the value of the effective source terms was varied parameterically to determine its impact on microstructural evolution [8]. A more realistic representation of the physical processes that lead to vacancy production bias requires the incorporation of interstitials as a separate defect species, as well as vacancy-interstitial recombination and sinks for vacancies and interstitials. In addition, recent atomistic calculations have shown that it is incorrect to assume that Xe atoms sitting on monovacancy sites are the dominant defect species. At lower temperatures, athermal diffusion of interstitial Xe atoms is the dominant mechanism of Xe transport; at intermediate temperatures, the dominant defect is Xe bound to U_4O_3 clusters; and at high temperatures, the dominant defect is Xe bound to U_2O clusters [9].

In this section, a more realistic picture of the relevant defects is incorporated into the phase-field model of Ref. [8]. The effect of the incorporation of interstitials and the interstitial-vacancy recombination is considered in Section 2.1.1, and an approach to mimic the effect of interstitials by including an effective vacancy sink term is described. In Section 2.1.2, the effect of Xe bound to multi-vacancy clusters is considered. Finally, in Section 2.1.3, a value for the effective vacancy source term is determined—one that allows the growth rate of the simpler vacancy-only model to match that of the full interstitial-vacancy model.

2.1.1 Incorporation of interstitials

The evolution equations for fission gas bubble microstructure evolution in UO_2 were originally derived from a grand-potential functional presented in Ref. [8]. The evolution of each order parameter is given by the Allen-Cahn equation:

$$\frac{\partial \eta_{\alpha i}}{\partial t} = -L \frac{\delta \Omega}{\delta \eta_{\alpha i}} \tag{2.1}$$

where $\eta_{\alpha i}$ is the order parameter representing each phase (α indexes phases and i indexes grains), Ω is the total grand potential of the system, $\frac{\delta \Omega}{\delta \eta_{\alpha i}}$ is the variational derivative of Ω with respect to order parameter $\eta_{\alpha i}$, and L is the order parameter mobility, which generally is a function of order parameters and concentration. The Allen-Cahn equations are unchanged from Ref. [8].

The evolution equation for Xe atoms is given by

$$\frac{\partial \rho_g}{\partial t} = \nabla \cdot \left(M_g \nabla \mu_g \right) + s_g \tag{2.2}$$

where ρ_g is the number density of gas atoms, M_g is the mobility of gas atoms, μ_g is the chemical potential of gas atoms, and s_g is the source term for the production of gas atoms. $s_g = s_g^0 h_m$, where s_g^0 is the Xe production rate and h_m is a switching function that limits the production of gas atoms to the fuel matrix phase. The Xe production rate $s_g^0 = \dot{F} Y_{Xe}$, where $\dot{F}$ is the fission rate density and Y_{Xe} is the fission yield of Xe. In the grand potential model, Equation 2.2 is converted into an evolution equation for the chemical potential of ρ_g.

The evolution equation for vacancies was originally given as [8]

$$\frac{\partial \rho_v}{\partial t} = \nabla \cdot \left(M_v \nabla \mu_v \right) + s_v \tag{2.3}$$

with terms defined similarly as Equation 2.2, and $s_v = s_v^0 h_m$. In Ref. [8], s_v^0 was given as $s_v^0 = C\dot{F}$, where C is a constant ranging from 5 to 20.

To incorporate interstitials as an additional defect species, the evolution equation for vacancies was modified to

$$\frac{\partial \rho_v}{\partial t} = \nabla \cdot \left(M_{vv} \nabla \mu_v \right) + s_v - K_{iv} \rho_i \rho_v - K_{vs} \rho_v \tag{2.4}$$

where ρ_i is the number density of interstitials, K_{iv} is the recombination constant representing the strength of vacancy-interstitial recombination, and K_{vs} is the product of the vacancy sink strength and sink density. M_{vv} represents the mobility of vacancies in response to gradients in the vacancy chemical potential; it is the same value as the previously used M_v, but the double vv notation is introduced due to the presence of cross-coupling terms between different defects, as will be discussed further in Section 2.1.2. Again, this is converted into an evolution for chemical potential, using the process described in Ref. [10]. A similar evolution equation is introduced for interstitial number density:

$$\frac{\partial \rho_i}{\partial t} = \nabla \cdot \left(M_{ii} \nabla \mu_i \right) + s_i - K_{iv} \rho_i \rho_v - K_{is} \rho_i \tag{2.5}$$

The kinetic coefficients for Equations 2.4 and 2.5 are parameterized as follows. Each fission event is assumed to create 10^4 vacancy-interstitial pairs, thus $s_v^0 = s_i^0 = 10^4 \dot{F}$. The recombination constant and sink strengths are parameterized as follows. At low to intermediate temperatures, cluster dynamics simulations have shown that the steady-state normalized concentration of vacancies $c_v^{ss} \approx 0.008$. The corresponding steady-state number density $\rho_v^{ss} = 0.195$ nm^{-3}. When sink strengths are small compared to the recombination constant,

$$\rho_v^{ss} \approx \sqrt{\frac{s_v^0 K_{is}}{K_{iv} K_{vs}}} \tag{2.6}$$

Sinks such as dislocations preferentially absorb interstitials over vacancies, and the diffusion of interstitials is generally significantly greater than that of vacancies; thus typically $K_{is} \gg K_{vs}$. We assumed values of $K_{is} = 10^{-3}$ s^{-1} and $K_{vs} = 10^{-5}$ s^{-1}, and using Equation 2.6, chose the value for K_{iv} that gave $\rho_v^{ss} = 0.195$ nm^{-3}, resulting in $K_{iv} = 0.285$ nm^3/s.

Additionally, the chemical free energy density of the system was modified to account for the presence of interstitials. As for the vacancies and gas atoms, a parabolic approximation was assumed for the free energy's dependence on the interstitial concentration. The chemical free energy density of the matrix phase, $f_{m,chem}$, is given by

$$f_{m,chem} = \frac{1}{2}k_v^m(c_v - c_v^{m,eq})^2 + \frac{1}{2}k_g^m(c_g - c_g^{m,eq})^2 + \frac{1}{2}k_i^m(c_i - c_i^{m,eq})^2 \tag{2.7}$$

where k_j^m is the curvature of the parabola for the defect species j, c_j is the normalized concentration (mole fraction) of defect species j (related to number density ρ_j using $c_j = \rho_j / V_a$, where V_a is the atomic volume), and $c_j^{m,eq}$ is the minimum of the parabola with respect to concentration for species j. Similarly, for the bubble phase,

$$f_{b,chem} = \frac{1}{2}k_v^b(c_v - c_v^{b,eq})^2 + \frac{1}{2}k_g^b(c_g - c_g^{b,eq})^2 + \frac{1}{2}k_i^b(c_i - c_i^{b,eq})^2 \tag{2.8}$$

The parameters used for the full vacancy + interstitial simulations are summarized in Table 2.1. As in Ref. [8], the interface width l_{int} used was 30 nm, and grain boundary energy $\sigma_{mm} = 1.5$ J/m^2. From these values, the model parameters κ and m were determined using analytical expressions valid for $\gamma_{mimj} = 1.5$ [10]. The governing equations were non-dimensionalized using energy scale $E^* = 64$ J/m^3, length scale $l^* = 1$ nm, and time scale $\tau^* = 0.1$ s.

In addition to the full vacancy + interstitial model, a vacancy-only model that incorporates an effective sink term was also implemented. The purpose of the effective sink term was to cause the steady-state vacancy concentration in the matrix phase to match the value expected from the cluster dynamics simulations, similar to what is observed in the full vacancy + interstitial model but without the need to explicitly track the interstitial defects. The evolution equation for vacancies in the vacancy source + sink model is

$$\frac{\partial \rho_v}{\partial t} = \nabla \cdot \left(M_{vv} \nabla \mu_v \right) + s_v - K_{vs}^{eff} \rho_v \tag{2.9}$$

The effective sink term is parameterized such that, in the matrix, under steady-state conditions where $\nabla \mu_v = 0$,

Parameter	Value
V_a	0.0409 nm^3
E_v^f	3 eV
E_v^g	3 eV
E_v^i	3 eV
$c_g^{b,eq}$ (intergranular)	0.454
$c_v^{b,eq}$ (intergranular)	0.546
$k_v^m = k_g^m = k_i^m$	1.92×10^{10} J/m^3
$k_v^b = k_g^b = k_i^b$	9.0×10^{10} J/m^3
l_{int}	30 nm
κ	3.38×10^{-8} J/m
m	3.00×10^{8} J/m^3
γ_{mimj}	1.5
$\theta/2$	50°
γ_{mib0}	0.922
$\dot{F}$	1.09×10^{13} fissions/(cm^3 s)
Y_{Xe}	0.2156
s_g^0	2.35×10^{12} atoms/(cm^3 s)
$s_v^0 = s_i^0$	1.09×10^{17} defects/(cm^3 s)
D_g	0.1 nm^2/s
D_v	0.1 nm^2/s
D_i	10 nm^2/s
K_{iv}	0.285 nm^3/s
K_{is}	10^{-3} s^{-1}
K_{vs}	10^{-5} s^{-1}
L	1.56×10^{-11} m^3/(J s)

Table 2.1. Parameters used for full vacancy + interstitial phase-field simulations.

$\rho_v = \rho_v^{ss} = 0.195$ nm^{-3}, as per Ref. [9]. Using Equation 2.9, when $\nabla \mu_v = 0$ and $\frac{\partial \rho_v}{\partial t} = 0$,

$$K_{vs}^{eff} = \frac{s_v}{\rho_v^{ss}} \tag{2.10}$$

resulting in $K_{vs}^{eff} = 5.58 \times 10^{-4}$ s^{-1}.

To compare the growth rates of the bubble phase when using the three different models (vacancy source, vacancy source + sink, vacancy + interstitial), pseudo-1-D simulations were performed, with a domain size of 500 nm in the x-direction and 20 nm in the y-direction. The simulation domain was discretized using linear Lagrange finite elements using the MOOSE framework; 50 elements and 2 elements were used in the x and y directions, respectively, resulting in a uniform mesh size $\Delta x = 10$ nm. This gives three elements across the 30-nm interface width in the x-direction, a resolution that has proven adequate for simulating growth processes when using this model [10].

The initial conditions for the simulations were a bubble-matrix interface at $x = 100$ nm, with the bubble phase in $x < 100$ and the matrix phase in $x > 100$. The initial conditions for the order parameters representing the bubble and matrix phases—η_{b0} and η_{m0}, respectively—were

$$\eta_{b0} = \frac{1}{2}\left[1 - \tanh\left(\sqrt{\frac{m}{2\kappa}}x\right)\right] \tag{2.11}$$

and

$$\eta_{m0} = \frac{1}{2}\left[1 + \tanh\left(\sqrt{\frac{m}{2\kappa}}x\right)\right] \tag{2.12}$$

(Note that the order parameter profiles in the bubble-matrix interface will be slightly wider than the initial width given by Equations 2.11 and 2.12 because the analytical expressions are derived for the parameter choice $\gamma = 1.5$ and the coefficient used for the bubble-matrix interface is $\gamma_{mib0} = 0.922$; however, the order parameters will rapidly adapt to their equilibrium widths within a few simulation time steps.) The initial chemical potentials for gas atoms, vacancies, and interstitials are all zero in the initial conditions.

The position of the interface as a function of time for the three different models is shown in Figure 2.1. The position of the interface is defined as the position where $\eta_{b0} = 0.5$, and is determined via interpolation of the finite element shape function for η_{b0}. For the vacancy source model, $C = 5$ was used. For all three models, the position of the interface shifts quickly just after the simulation begins. This is caused by the equilibration of η_{b0} in the initial time steps. The amount of the shift was significantly larger for the vacancy source + sink and vacancy + interstitial models, but still occurred for the vacancy source model as well. To determine if this rapid shift was related to the choice of $\gamma_{mib0} = 0.922$ and the use of Equations 2.11 and 2.12, the simulations were repeated with $\gamma_{mib0} = 1.5$. Although this reduced the amount of the initial shift in the interface positions, the shift was still significant. The interface shift is seemingly related to the source and sink term effects on the order parameter profiles. For the vacancy + sink and vacancy + interstitial models, as the source and sink terms come into steady-state and ρ_v approaches ρ_v^{ss}, the interface position shifts significantly. This initial shift should be accounted for in the initial conditions for phase-field simulations, as it can significantly impact the initial sizes of bubbles set in the initial conditions. However, following this initial shift in interface position, both the vacancy source + sink and vacancy + interstitial models show the same steady-state growth rates. Thus, the

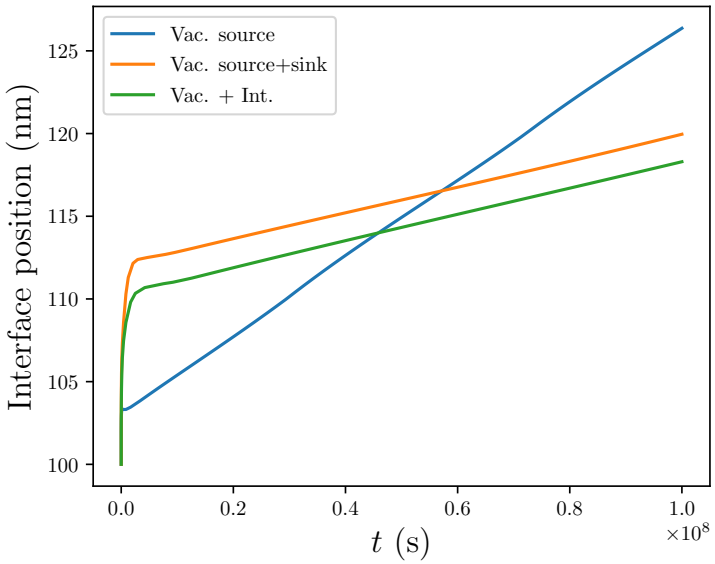

Figure 2.1. Growth of bubble phase as a function of time using the vacancy source, vacancy source + sink, and vacancy + interstitial models. After the initial interface equilibration, the steady-state growth rate predicted by the vacancy source + sink and vacancy + interstitial models match, while the vacancy source model (with $C = 5$) overpredicts the growth rate.

vacancy source + sink model can correctly match the steady-state growth rate of the vacancy + interstitial model at a reduced computational cost. The vacancy source model with $C = 5$, the lowest of the values used previously [8], still significantly overpredicts the steady-state growth rate.

2.1.2 Incorporation of multi-vacancy clusters

At higher temperatures, the most mobile Xe defect is a Xe atom bound to a U_2O cluster [9], meaning that each gas atom transported to a bubble brings U-site vacancies. Equation 2.2 for the transport of Xe accounts for one of the two vacancies, since the model assumes Xe atoms are on U lattice sites. To account for the additional vacancy, a coupling term is added to the evolution equation for vacancies:

$$\frac{\partial \rho_v}{\partial t} = \nabla \cdot \left(M_{vv} \nabla \mu_v + M_{vg} \nabla \mu_g \right) + s_v - K_{iv} \rho_i \rho_v - K_{vs} \rho_v \tag{2.13}$$

The $M_{vg} \nabla \mu_g$ added to the right-hand side represents a flux of vacancies that is proportional to the gradient in the chemical potential. For a two-vacancy cluster, $M_{vg} = M_{gg}$ so that the transport of one additional vacancy will occur at the same rate as the gas atom transport.

The growth of the bubble phase was simulated using a pseudo-1-D domain, as described in Section 2.1.1, using Equation 2.13 instead of Equation 2.4 for vacancy evolution. The simulation results are shown in Figure 2.2. The growth rate accounting for the multi-vacancy transport with the coupling term $M_{vg} \nabla \mu_g$ was nearly identical to that of

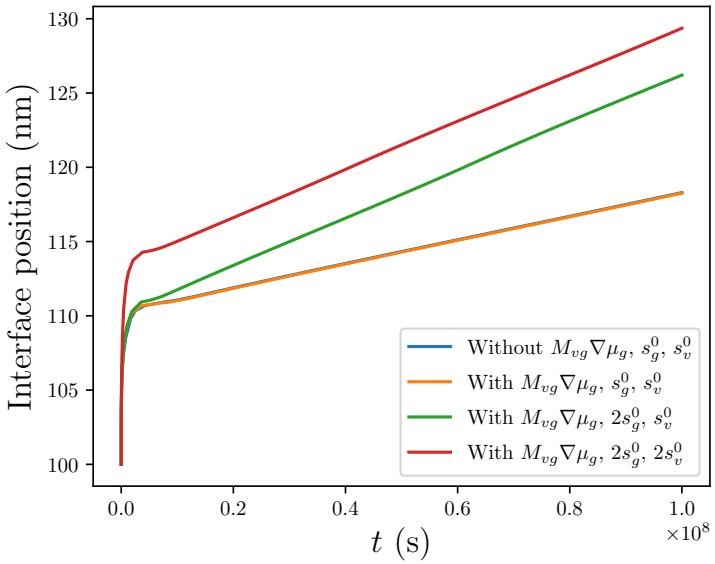

Figure 2.2. Growth of bubble phase as a function of time both without and with the coupling term $M_{vg}\nabla\mu_g$ to account for multi-vacancy clusters. The growth rate is nearly identical both without and with the coupling term, because an excess of vacancies always exists in the matrix, such that the defect concentrations in the bubble phase are maintained at equilibrium, and the growth rate is controlled by the gas source term strength. To demonstrate this, doubling the gas source term strength to $2s_g^0$ also doubled the steady-state growth rate.

the rate without the coupling term. It is believed that the coupling term does not affect the growth rate because in the vacancy + interstitial model, there is always an excess of vacancies in the matrix phase. The bubble phase can therefore draw as many vacancies as are needed to maintain the bubble phase at its equilibrium composition. When the coupling term is present, it causes more vacancies to be transported to the bubble phase; therefore, fewer vacancies are drawn from the excess in the matrix phase by the M_{vv} term. If this is correct, the growth rate of bubbles is controlled by the gas atom flux. To confirm this understanding, growth with the gas source term strength doubled to $2s_g^0$ was simulated. As seen in Figure 2.2, doubling the gas source term strength caused the growth rate to double, confirming that the gas source term strength controls the growth rate because sufficient vacancies are always present to keep the growing bubble in equilibrium. To further improve this understanding, the vacancy and interstitial source terms were doubled as well. In that case, the steady-state vacancy concentration is expected to increase by a factor of $\sqrt{2}$ by Equation 2.6. As seen in Figure 2.2, although the initial shift in interface position at early times is greater, once the steady-state interfacial profile is achieved, the steady-state growth rate is identical to that of the case with gas source term strength $2s_g^0$ and vacancy source strength s_v^0.

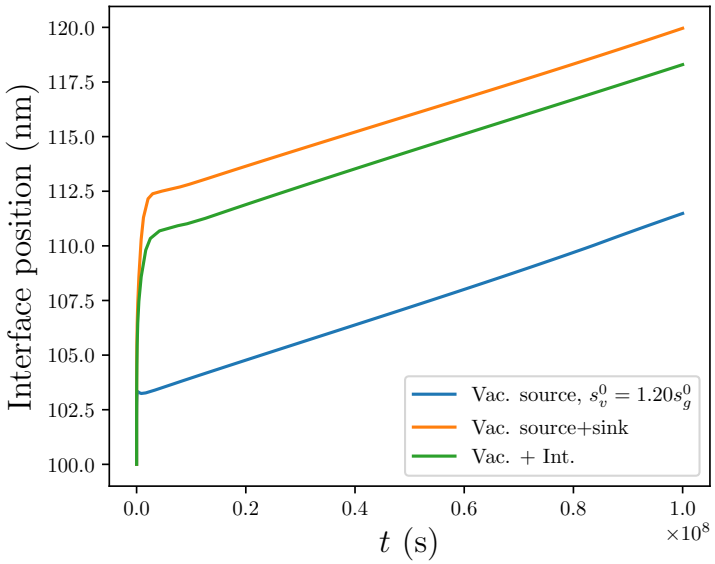

Figure 2.3. Growth rate of vacancy source model with $C = 1.20$ compared to the growth rates of the vacancy + interstitial and vacancy source + sink models. After the initial interface equilibration, the steady-state growth rates are identical.

2.1.3 Determination of an effective vacancy source term to match the full interstitial-vacancy model

In Section 2.1.1, it was shown that using the vacancy source model with $C = 5$ caused the growth rate to be overestimated. In this section, the value of C that allows the vacancy source model to match the vacancy + interstitial model is determined. The free energy of the gas bubble phase is given by a parabolic approximation to the Helmholtz free energy of a van der Waals gas; as seen in Table 2.1, the minima of the parabolic approximation is at $c_g^{b,eq} = 0.454$ and $c_v^{b,eq} = 0.546$. The equilibrium compositions of gas bubble-solid equilibrium are determined by the common tangent plane construction for a ternary system. Assuming the composition does not deviate significantly from the minima of the parabolic approximation, the ratio of vacancies to gas bubbles is $c_v^{b,eq}/c_g^{b,eq} = 1.20$. To maintain that ratio, $C = 1.20$ can be set. Growth of the bubble phase using the vacancy source model with $C = 1.20$ was simulated using the pseudo-1-D configuration described in Section 2.1.1. The growth rate is shown in Figure 2.3 and then compared to the vacancy + interstitial and vacancy source + sink models. After the initial equilibration of the interfaces, the growth rate of the vacancy source model with $C = 1.20$ is in good agreement with the other models. The initial shift in interface position is also smaller with the vacancy source model, and this is advantageous for setting initial conditions because a large shift in initial interface position need not be accounted for. However, note that these results were achieved with a bubble phase whose initial conditions were close to chemical equilibrium, with $c_b = 0.454$ and $c_v = 0.546$ in the bubble phase at $t = 0$. This approach may not work as well for bubbles whose initial conditions significantly differ from chemical equilibrium.

2.2 Bubble evolution in the fully formed HBS region

Phase-field modeling is a well-established state-of-the-art approach for capturing microstructural evolution at the mesoscale. It has been employed to capture microstructural evolution in nuclear environments, including defect evolution, fission gas bubble formation, and grain growth. In previous years, a grand-potential-based phase-field model was developed to capture HBS formation and associated bubble evolution [7]. The model predicts the growth of existing bubbles and the formation of new inter-granular and intra-granular bubbles, due to the gas supersaturation in the matrix. However, some of these bubbles physically appear at a lower length scale, presenting numerical challenges for mesoscale simulations. Additionally, due to lack of information on defect evolution in HBS regions, including intra-granular fission gas behavior, the phase-field model alone fails to capture the fission gas evolution in HBS regions. To mitigate this, a coupled phase-field and spatially resolved cluster-dynamics model was developed. In this approach, the intra-granular fission gas behavior is captured by the cluster dynamics code Xolotl, while the microstructural evolution, including the evolution of grains and inter-granular fission gas bubbles are handled by the phase-field model. This hybrid approach can appropriately resolve the fission gases at the lower length scale while still capturing their impact on bubble growth and overall microstructural evolution. This approach was first developed for capturing fission gas release behavior in nuclear fuel during normal operating conditions [11]. Here, we adapt the approach for HBS conditions. This year, we utilized the hybrid model to capture bubble growth and pressure evolution in fully formed HBS regions.

In this section, we provide a brief account of the hybrid approach and summarize the governing equations for both the phase-field and cluster-dynamics models, along with the strategy for coupling the two. We also provide details on parameterizing the model for HBS conditions in light-water reactors. The model accounts for existing fission gas bubbles and concurrently tracks the concentration of defects such as vacancies and gas atoms, leading to further bubble growth and pressure increases. Additionally, it considers the role of defect sources, defect recombination, various diffusion mechanisms, and activation paths that contribute to the formation of new bubbles and the coalescence of the smaller bubbles into the larger ones. The model predicts the growth of existing bubbles and the formation of new inter-granular ones.

2.2.1 Description of the coupled cluster-dynamics and phase-field model

2.2.1.1 Phase-field model formulation

The HBS bubble growth model presented in this section was formulated by following the grand-potential-based multi-order parameter, multi-component phase-field model. This model can concurrently capture the evolution of multiple phases, grains, and chemical species. It has previously been applied to model phase separation, solidification, and the sintering of complex alloy systems [12, 10, 13, 14]. Recently, Aagesen et al. [8, 15] applied the model to evaluate bubble evolution in various nuclear materials. In this model, the microstructure is considered to have two significant and distinguishable crystallographic features: the solid matrix and the bubble phases. Within the matrix, multiple grains are represented by using different order parameters, $\eta_{m0}, \eta_{m1}, \ldots \eta_{mi}, \ldots \eta_{mn}$, while the bubbles are represented by a single order parameter, η_b. Additionally, local concentrations of various defect species such as vacancies and fission gases are represented as chemical components, the number densities of which are represented by ρ_v and ρ_g,

respectively.

The evolution of the order parameters is captured using the Allen-Cahn equations derived from the grand potential functional, such that:

$$\begin{aligned} \frac{\partial \eta_{mi}}{\partial t} &= -L_m \frac{\delta \Omega}{\delta \eta_{mi}} \\ \frac{\partial \eta_b}{\partial t} &= -L_b \frac{\delta \Omega}{\delta \eta_b}, \end{aligned} \tag{2.14}$$

where L_m and L_b are the kinetic mobility of the order parameters, and $\frac{\delta \Omega}{\delta \eta_{mi}}$ and $\frac{\delta \Omega}{\delta \eta_b}$ are the variational derivatives of the grand potential Ω with respect to the order parameters η_{mi} and η_b, respectively. The total grand potential of the system, Ω, is derived from the local grand-potential density as:

$$\Omega = \int_V \left(\omega_{bulk} + \omega_{grad} + \omega_{chem} \right) \mathrm{d}V \,, \tag{2.15}$$

where ω_{bulk} accounts for the bulk free energy density term, ω_{grad} adds the gradient energy contribution, and ω_{chem} incorporates the appropriate grand-potential densities for each phase. Each of these components is defined as follows:

$$\omega_{bulk} = \alpha \left[\left(\frac{\eta_b^4}{4} - \frac{\eta_b^2}{2} \right) + \sum_{i=1}^{n_m} \left(\frac{\eta_{mi}^4}{4} - \frac{\eta_{mi}^2}{2} \right) + \left(\frac{\gamma_{bm}}{2} \eta_b^2 \sum_i \eta_{mi}^2 + \sum_i^{n_m} \sum_{i \neq j}^{n_m} \frac{\gamma_{mm}}{2} \eta_{mi}^2 \eta_{mj}^2 \right) + \frac{1}{4} \right], \tag{2.16}$$

$$\omega_{grad} = \frac{\kappa}{2} \left(|\eta_b|^2 + \sum_{i=1}^{n_m} |\nabla \eta_{mi}|^2 \right), \tag{2.17}$$

and

$$\omega_{chem} = h_b \omega_b + h_m \omega_m \,, \tag{2.18}$$

where m and b represent the matrix and bubbles phases, i and j are indices for the grains, n_m is the total number of grains, and α is a constant free energy barrier coefficient. γ_{mb} and γ_{mm} are constant parameters that allow adjustment of interfacial energies between phases and grains. The model assumes isotropic interfacial properties without considering inclination or misorientation dependence. $\left(\frac{\alpha}{4} \right)$ is added to make the homogeneous free energy density equal 0 within grain interiors. κ is the gradient energy coefficient. ω_m and ω_b represent the local grand-potential density of the matrix and bubbles phases, respectively, and h_m and h_b are the switching functions used for interpolating the grand-potential density between the phases. For the matrix and bubble phases, the switching functions are:

$$h_m = \frac{\sum_{i=1}^{n_m} \eta_{mi}^2}{\eta_b^2 + \sum_{i=1}^{n_m} \eta_{mi}^2} \tag{2.19}$$

and

$$h_b = \frac{\eta_b^2}{\eta_b^2 + \sum_{i=1}^{n_m} \eta_{mi}^2} \,, \tag{2.20}$$

respectively.

The evolution of the vacancies and gas atoms is expressed in terms of the chemical potentials μ_v and μ_g, such that:

$$\frac{\partial \mu_g}{\partial t} = \frac{1}{\chi_g}\left[\nabla \cdot \left(D_g \chi_g \nabla \mu_g\right) + s_g - \frac{\partial \rho_g}{\partial \eta_b}\frac{\partial \eta_b}{\partial t} - \sum_{i=1}^{n_m} \frac{\partial \rho_g}{\partial \eta_{mi}}\frac{\partial \eta_{mi}}{\partial t}\right] \tag{2.21}$$

and

$$\frac{\partial \mu_v}{\partial t} = \frac{1}{\chi_v}\left[\nabla \cdot \left(D_v \chi_v \nabla \mu_v\right) + s_v - \frac{\partial \rho_v}{\partial \eta_b}\frac{\partial \eta_b}{\partial t} - \sum_{\alpha}\sum_{i=1}^{p_\alpha} \frac{\partial \rho_v}{\partial \eta_{\alpha i}}\frac{\partial \eta_{\alpha i}}{\partial t}\right], \tag{2.22}$$

where D_g and D_v are the diffusion coefficients, and s_g and s_v are the source terms for the production of Xe atoms and U site vacancies, respectively. χ_g and χ_v are the susceptibilities defined as:

$$\chi_g = h_m \frac{1}{V_a^2 k_g^m} + h_b \frac{1}{V_a^2 k_g^b} \tag{2.23}$$

and

$$\chi_v = h_m \frac{1}{V_a^2 k_v^m} + h_b \frac{1}{V_a^2 k_v^b}, \tag{2.24}$$

respectively. The grand-potential density for each phase is given by:

$$\omega_m = f_m - \mu_g \rho_g - \mu_v \rho_v \tag{2.25}$$

and

$$\omega_b = f_b - \mu_g \rho_g - \mu_v \rho_v\,, \tag{2.26}$$

where f_m and f_b are the Helmholtz free energies of each phase and μ_g and μ_v are the chemical potentials of the gas atoms and vacancies. The free energy of both phases are approximated as parabolic functions of vacancy and gas concentration, such that:

$$f_m = \frac{1}{2}k_v^m (c_v - c_v^{m,eq})^2 + \frac{1}{2}k_g^m (c_g - c_g^{m,eq})^2 \tag{2.27}$$

and

$$f_b = \frac{1}{2}k_v^b (c_v - c_v^{b,eq})^2 + \frac{1}{2}k_g^b (c_g - c_g^{b,eq})^2, \tag{2.28}$$

where k_v^m and k_g^m are the curvatures of the parabolas and $c_v^{m,eq}$ and $c_g^{m,eq}$ represent the equilibrium concentration of vacancies and gas atoms in the UO_2 matrix, respectively. The curvatures of these parabolic functions were derived from the equivalency of the ideal energy form for the respective phases. Details on this approach are provided in [7].

Here, we describe the interfacial parameterization of the model for HBS formation in UO_2 at 1200 K. The energy density, length, and time scales used for non-dimensionalizing the model are 1 eV/nm^3, 1 nm, and 1 second, respectively. The grain boundary energy of UO_2 is considered to be $\sigma_{mm} = 1.5$ J/m^2 or 9.363 eV/nm^2. The interfacial energy between the matrix and gas bubble phase is considered to be the same as the grain boundary energy (i.e., $\sigma_{mb} = \sigma_{mm}$). This indicates a dihedral angle of 120° between the bubbles and the grain boundaries. The interfacial properties were

calculated by assuming an interface thickness of $l_{int} = 10$ nm. The free energy coefficients were obtained via [16]:

$$\alpha = \frac{6\sigma_{mm}}{l_{int}} \tag{2.29}$$

and

$$\kappa = \frac{3}{4}\sigma_{mm} l_{int}\,. \tag{2.30}$$

The kinetic mobility of the grains was obtained via:

$$L_m = \frac{4M_{GB}}{3l_{GB}}, \tag{2.31}$$

where M_{GB} is the grain boundary mobility:

$$M_{GB} = M_0 \exp\left(-\frac{Q}{k_B T}\right), \tag{2.32}$$

where $M_0 = 9.21 \times 10^{-9}$ m^4/Js, $Q = 3.01$ eV [17], and k_B is the Boltzmann constant. For the bubble-matrix interface, the kinetic mobility is defined such that the bubble evolution is solely diffusion controlled. To this end, the kinetic mobility of the bubble phase is increased until the bubble evolution is unaffected by the mobility value, as shown in Figure 2.4. Thus, the kinetic mobility of the bubble phase is considered to be $L_b = 10\,L_m$. Table 2.2 summarizes the model parameters, with sample values for 1200 K.

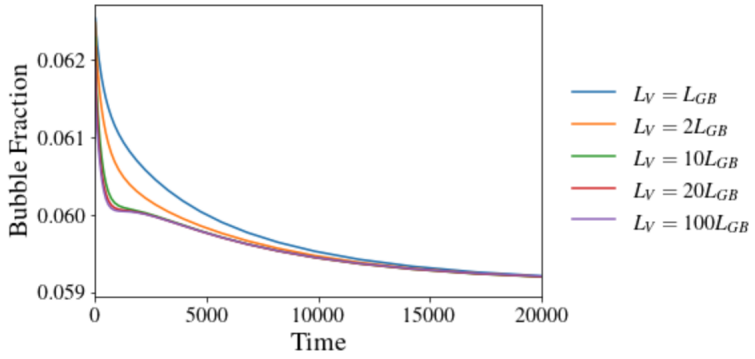

Figure 2.4. Kinetic mobility of the bubble phase, as determined to ensure diffusion-controlled bubble evolution.

2.2.1.2 Cluster dynamics model

The cluster-dynamics code Xolotl captures the evolution of the intra-granular fission gases [11]. It considers Xe as the primary fission gas present in the system and does not explicitly model vacancy evolution. The evolution of the Xe cluster is represented by:

$$\frac{\partial C_n}{\partial t} = \dot{F} y_n + D_n \nabla^2 C_n - Q(C_n)\,, \tag{2.33}$$

Parameter	Formulation	Value	Source
T		1200 K	
V_a		0.04092 nm^3	[18]
E_f^v		3 eV	[8]
E_f^g		3 eV	[8]
$c_{v/g}^{m,eq}$	$\exp\left(-\frac{E_v^f}{k_B T}\right)$	2.515×10^{-13}	[7]
k_v^m	$7335\,\mathrm{eV/nm^3} - 0.9682\,T\,\mathrm{eV/nm^3/K}$	6173.17 eV/nm^3	[7]
k_g^m	$3667.5\,\mathrm{eV/nm^3} - 0.41\,T\,\mathrm{eV/nm^3/K}$	3175.5 eV/nm^3	[7]
$c_v^{b,eq}$		0.562	[7]
$c_g^{b,eq}$		0.438	[7]
$k_{v/g}^b$	$0.2328\,T\,\mathrm{eV/nm^3/K} - 30.723\,\mathrm{eV/nm^3}$	245 eV/nm^3	[7]
l_{int}		10 nm	
σ_{mm}		1.5 J/m^2 or 9.363 eV/nm^2	
κ	$\frac{3}{4}\sigma_{mm} l_{int}$	1.125×10^{-8} J/m or 70.2 eV/nm	[7]
α	$\frac{6\sigma_{mm}}{l_{int}}$	9×10^8 J/m^3 or 5.62 eV/nm^3	[7]
f_0	$4.9 \times 10^{-3}\,T\,\mathrm{eV/nm^3/K} - 0.58\,\mathrm{eV/nm^3}$	5.316 eV/nm^3	[7]
G		64.1 GPa	[19]
M_{GB}	$9.21 \times 10^{-9} \exp\left(-\frac{3.01}{k_B T}\right)$ m^4/Js	3.43×10^{-4} nm^4/eV/s	[7]
L_{GB}	$\frac{4 M_{GB}}{3 l_{int}}$	4.58×10^{-5} nm^3/eV/s	[7]
L_b	$10L$	4.58×10^{-4} nm^3/eV/s	Section 2.2.1.1
S_v	$1.2 S_g$		Section 2.2.2.4
D_g^m	Eq. 2.41	0.0175 nm^2/s	Section 2.2.2.2
D_g^b	$10000\ D_g^m$	175 nm^2/s	Section 2.2.2.2
D_g^s	$1000\ D_g^m$	17.5 nm^2/s	Section 2.2.2.2
D_g^{GB}	$10000\ D_g^m$	175 nm^2/s	Section 2.2.2.2
D_v^m	$D_{v_U} = 2 \times 10^{-3} \exp(-2.4/k_B T)$ cm^2/s	16.65 nm^2/s	Section 2.2.2.2
D_v^b	$100\ D_g^m$	1665.27 nm^2/s	Section 2.2.2.2
D_v^s	$10\ D_g^m$	166.527 nm^2/s	Section 2.2.2.2
D_v^{GB}	$100\ D_g^m$	1665.27 nm^2/s	Section 2.2.2.2

Table 2.2. Parameters used for phase-field simulations of bubble evolution in HBS.

where C_n is the concentration of the cluster containing n Xe atoms, $\dot{F}$ is the fission rate, y_n is the fission yield of the Xe atoms, and D_n is the diffusion coefficient of a given cluster. The time evolution of the clusters consists of the production of new Xe, the diffusion of a single Xe atom, the clustering of Xe to form intra-granular bubbles, and the re-solution of Xe monomers. In this model, only single Xe atoms (i.e., Xe monomers) are considered mobile. The general reaction term for a cluster of size $n \geq 2$ is:

$$Q(C_n) = k_n C_n C_1 - k_{k-1} C_{n-1} C_1 + k_n^{emit} C_n - k_{n+1}^{emit} C_{n+1} + k_n^{reso} C_n - k_{n+1}^{reso} C_{n+1}, \tag{2.34}$$

with the following reaction rates:

$$k_n = 4\pi D_1 (r_1 + r_n), \tag{2.35}$$

$$k_{n+1}^{emit} = \frac{k_n}{V_a} \exp\left(\frac{-E_b}{k_B T}\right), \tag{2.36}$$

$$k_n^{reso} = \left(a_1 \exp\left(-b_1 r_n\right) + \frac{y(0) - a_1}{1 + c r_n^2} \exp\left(-b_2 r_n^2\right)\right) 10^4 \dot{F}. \tag{2.37}$$

Here, D_1 is the single Xe diffusion coefficient, r_n is the reaction radius for a bubble consisting of n Xe atoms, V_a is the atomic volume, E_b is the binding energy of Xe_{n+1}, k_B is the Boltzmann constant, and T is the temperature. The reaction term for a single Xe atom sums the contributions from each reaction, such that:

$$Q(C_1) = \sum_{n \geq 2} \left[k_n C_n C_1 - k_{n+1}^{emit} C_{n+1}\right] + 2k_1 C_1^2 - k_2^{emit} C_2 - 2k_2^{reso} C_2. \tag{2.38}$$

2.2.1.3 Implementation of the coupling approach

To implement and numerically solve the current model, we utilized the open-source parallel Multiphysics Object Oriented Simulations Environment (MOOSE) framework. A MOOSE-based wrapper application was designed to connect Xolotl to the phase-field model in MOOSE. MOOSE is a fully coupled, fully implicit finite element solver with adaptive time stepping and adaptive meshing capabilities. It utilizes the PETSc solver library and the vast finite element library from LibMesh. For the phase-field simulations, the finite element meshes were comprised of four-node quadrilateral elements (QUAD4). Meshes were generated using the internal MOOSE mesh generator, and linear Lagrange shape functions were used for all the nonlinear variables. The system of nonlinear equations was solved via the preconditioned Jacobian-free Newton-Krylov (PJFNK) [20] method. We employed the additive Schwarz method (ASM) for preconditioning and iterative LU factorization for sub-preconditioning. The simulations were solved with a linear tolerance of 1×10^{-3}, a nonlinear relative tolerance of 1×10^{-6}, and a nonlinear absolute tolerance of 1×10^{-8}. Automatic residual scaling was utilized to minimize any disparities in the residual norms corresponding to different nonlinear variables. For the time integration, an implicit time integration scheme with a second-order backward differentiation formula was employed. Furthermore, adaptive meshing and time stepping schemes were used to reduce the computational cost. The mesh was refined around the interface and coarsened in the other areas. This was achieved by refining the mesh in regions of high curvature in the order parameter fields, with the help of a gradient jump indicator scheme [21] within

MOOSE. The element sizes ranged from 6.25 to 50.0 nm, with three levels of mesh refinement/coarsening. Further mesh refinement did not impact the microstructural evolution. This adaptive meshing scheme allows us to appropriately resolve the interface without significantly increasing the computational cost. Additionally, an iteration-based time adaptivity scheme was employed to increase the time step, based on the number of iterations required to solve the coupled equation system. The optimal iteration window of 6±1 was adopted, and periodic boundary conditions were used to eliminate any boundary effect on the solution.

Xolotl uses a finite difference modeling approach to discretize the simulation domain, and employs PETSc-based implicit time integration schemes and solvers to solve the partial differential equations (PDEs). Xolotl utilizes a uniform grid spacing of 6.25 nm. The wrapper application directly copies the mesh into a MOOSE mesh and transfers the Xolotl solution at each grid point. While the interconnection between the phase-field model and the wrapper app is achieved through the loosely coupled MultiApp system, Xolotl solves for the intra-granular fission gas evolution and calculates the concentration of the Xe monomers arriving at the grain boundaries. This is added as the gas source term in the phase-field model. Figure 2.5 shows a schematic of the coupling approach.

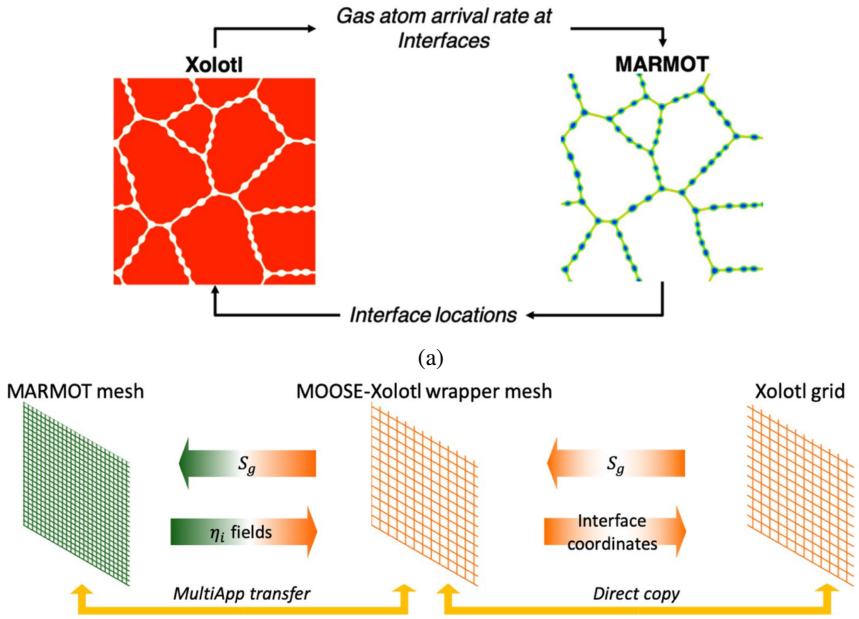

Figure 2.5. Schematic of the coupled approach: (a) transfer of physical quantities, and (b) strategy for transferring data between the applications [11].

2.2.2 Model characteristics

2.2.2.1 Initial condition generation

Here, we consider the bubble growth in completely recrystallized HBS. For this, a representative microstructure with periodic boundary conditions was created using a Voronoi tessellation with randomly specified existing bubbles. In this case, a simulation domain sized $1.25 \times 1.25\mu$m was considered. The simulation domain was initialized using 100 grains with a 125 nm average radius, and a single bubble with varying radii of 100, 150, or 200 nm, corresponding to approximately 2, 4.5, and 8% porosity, respectively. The initial conditions created for this set of simulations are shown in Figure 2.6.

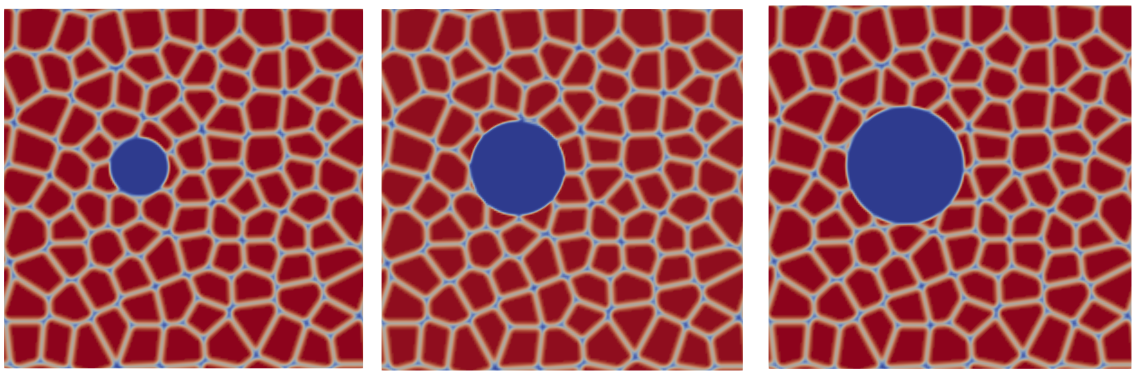

(a) (b) (c)

Figure 2.6. Sample initial HBS structure created via a Voronoi tessellation with (a) 100, (b) 150, and (c) 200 nm bubbles.

At the initial conditions, the bubble is considered to maintain equilibrium pressure, as determined by the Gibbs-Thomson condition, $P_{eq} = 2\gamma_{st}/r$, where γ_{st} is the surface tension and r is the bubble radius. Assuming $\gamma_{st} = \gamma$, the equilibrium pressure for the bubble sizes considered are 30, 20, and 15 MPa. The initial gas concentration within the bubble was estimated from the van der Waals equation of state:

$$P_g = \frac{c_g k_B T}{\Omega - c_g b}. \tag{2.39}$$

Thus, at 1200 K, the initial gas concentration within the bubble was set at 0.0642, 0.0448, and 0.0344 for the 100, 150, and 200 nm bubbles, respectively. The corresponding vacancy concentration within each bubble was set such that $c_v = 1 - c_g$. The initial matrix supersaturation value was obtained from Xolotl. To this end, a 0-D standalone Xolotl simulation was run until the time HBS was formed. The Xe retained at the end of the 0-D simulation was utilized to generate the intra-granular Xe distribution in the 2-D Xolotl simulation, which was then transferred to the phase-field simulations. The Xe concentration at the GB was set to zero at the initial condition. Single Xe atoms produced via intra-granular mechanisms were added to the GB as the simulation progressed. Figure 2.7 shows the steps used to generate the initial Xe supersaturation in the matrix. Figure 2.8 depicts the concentration of Xe monomers within the

grains, along with the single Xe atoms arriving at the GB at the initial time step.

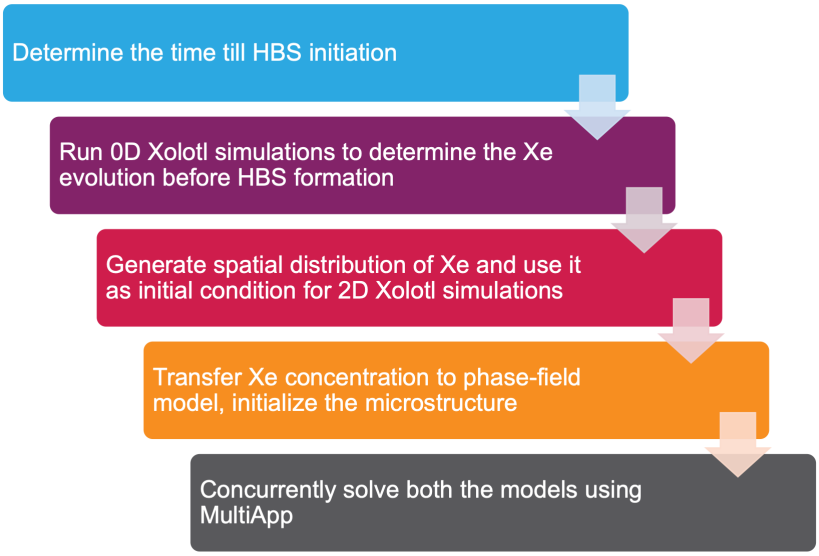

Figure 2.7. Schematic of the steps followed to generate the initial gas supersaturation in the matrix.

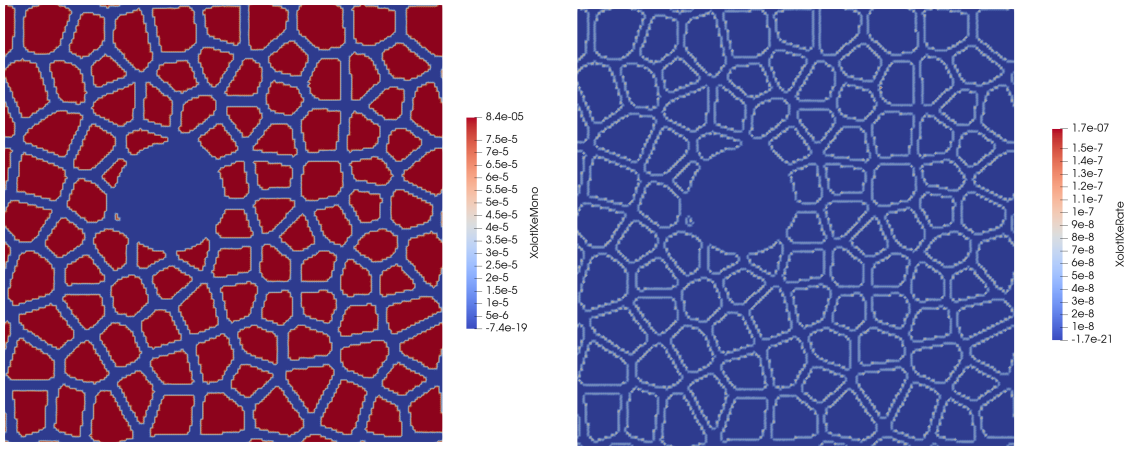

(a) (b)

Figure 2.8. (a) Initial Xe monomer concentration within grains. (b) The Xe source arriving at the GB at the initial condition for the 150 nm bubble case.

2.2.2.2 Effect of diffusion coefficients

Diffusion of U-vacancies and U-substitutional Xe gas atoms plays a pivotal role in dictating bubble growth and pressure increases. Under temperatures at which HBS is dominant, diffusion is usually athermal and driven by irradiation. There

are very limited data on the diffusion coefficients for vacancies and gas atoms at low temperatures. Perriot et al. [22] derived diffusion values considering the mobilities of different Xe clusters. The diffusivity values obtained from the cluster dynamics simulations are fitted such that:

$$D_g = D_1(T) + D_2(T, \dot{F}) + D_3(\dot{F}) \tag{2.40}$$

$$D_1(T) = \frac{2.22 \times 10^{-7} \exp(-3.26/k_B T)}{1 + 29.0 \exp(-1.84/k_B T)} \tag{2.41}$$

$$D_2(T, \dot{F}) = 2.82 \times 10^{-22} \exp(-2.0/k_B T)\sqrt{\dot{F}} \tag{2.42}$$

$$D_3(\dot{F}) = 8.5 \times 10^{-40} \dot{F}, \tag{2.43}$$

where D_g is in units of m^2/s. For a typical light-water reactor fission rate density of 1.09×10^{19} fissions/m^3-s and a temperature of 1200 K, the gas diffusion value is 1.75×10^{-20} m^2/s, or 0.0175 nm^2/s. For 1100, 1000, and 900 K, the values are 1.02×10^{-2}, 9.35×10^{-3}, and 9.27×10^{-3} nm^2/s, respectively. Below 900 K, athermal diffusion dominates, and the diffusivity value of 9.27×10^{-3} nm^2/s persists. For the coupled simulations, this D_g value is used as the bulk diffusion coefficient for the gas atoms within the grain interiors in both the Xolotl and phase-field simulations. The phase-field model uses enhanced diffusion coefficients within the bubbles, along the grain boundaries and the bubble surfaces. Olander [23] showed that Xe diffusivity along GBs can be 10–10,000 times faster than the bulk diffusivity reported by Turnbull [24]. Various Xe diffusivity values reported in the literature are shown in Figure 2.9.

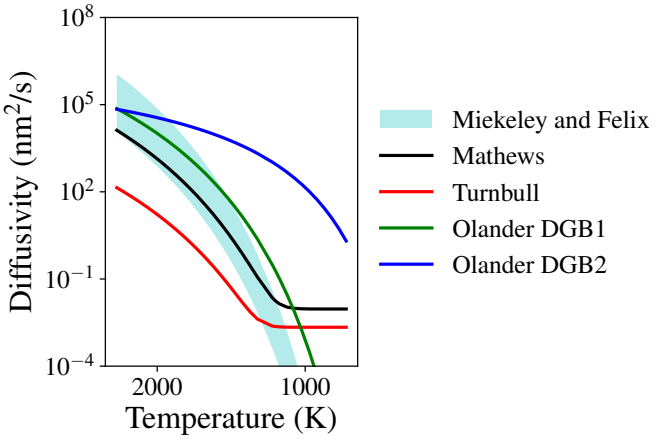

Figure 2.9. Bulk and GB diffusivity of Xe atoms in UO_2.

For the vacancy diffusion coefficients, we used the irradiation-enhanced values reported by Matzke [25]: $D_{v_U} = 2 \times 10^{-3} \exp(-2.4/k_B T)$ cm^2/s. At 1200 K, this yields a vacancy diffusion value of 16.653 nm^2/s. We set the lower limit on the diffusivity at the irradiation-enhanced value of 1.677 nm^2/s. The steady-state vacancy concentration in the matrix is considered to be 0.008 atomic fraction [9]. Furthermore, enhanced diffusion along the GBs and bubble surfaces is considered to accelerate the gas and vacancy transport in the HBS regions. Diffusion of both vacancies and

gas atoms follows the following relation:

$$D = D_m h_m + D_b h_b + 30 D_s \eta_b^2 (1-\eta_b)^2 + 9 D_{gb} \sum_i \sum_{j \neq i} \eta_{mi}^2 \eta_{mj}^2, \tag{2.44}$$

where D_m is the bulk diffusion coefficient in the matrix, D_b is the diffusion coefficient within bubbles, D_s is the coefficient for surface diffusion, and D_{gb} is the coefficient of diffusion along grain boundaries. This expression is used to incorporate the effect of different diffusion mechanisms in the model. Since the physical diffusion values in the different microstructural regions are unknown, we vary the enhancement factors and study their effect on bubble growth. Figure 2.10 depicts the effect of enhanced diffusion on inter-granular bubble evolution, leading to a change in porosity. The growth rate of the existing bubbles accelerates in correlation with the added diffusion enhancement factors. It was previously noted that these diffusion enhancement factors also influence the formation of new bubbles vs. the growth of existing bubbles in the HBS regions [26]. With the current hybrid model, we can concurrently capture the growth of existing bubbles and the formation of new inter-granular bubbles, while also limiting numerical issues. Note that the computational cost increases with any increase in enhancement factors. The finalized diffusion enhancement factors used in the pressure calculation simulations are reported in Table 2.2.

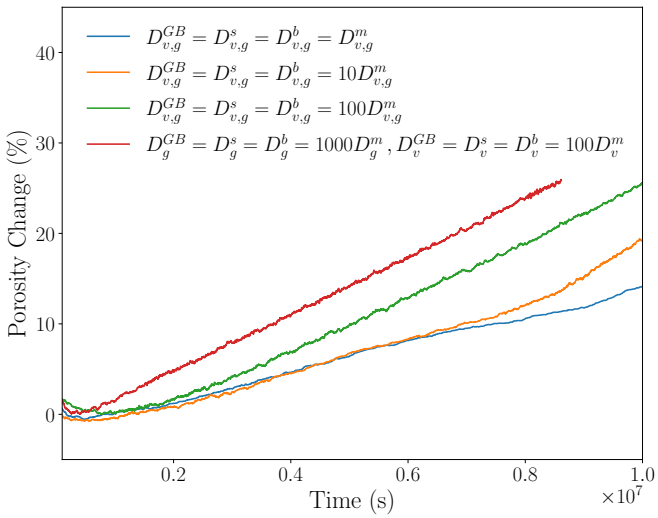

Figure 2.10. Effect of enhanced diffusion on inter-granular bubble growth.

2.2.2.3 Role of different intra-granular mechanisms

The cluster dynamics simulations in Xolotl consider the production, diffusion, clustering, and re-solution of Xe atoms within the grain interiors. Each of these mechanisms could potentially influence the evolution of the inter-granular bubbles captured by the phase-field model. To study the effect of each mechanism, we simulated the bubble growth in the HBS region at 1200 K by activating each mechanism one at a time. No initial gas supersaturation was consid-

ered in this case. Figure 2.11 demonstrates the effect of various intra-granular mechanisms on the evolution of the inter-granular bubble fraction. Figure 2.11a considers the usual HBS diffusivities with an enhancement factor of 100. Without clustering, all the Xe produced contributed to the bubble growth, while clustering limited the free single Xe atoms available in the system. However, when re-solution is considered, more Xe monomers are released, further contributing to the inter-granular bubble evolution. Figure 2.11b compares the no clustering case with the clustering and re-solution for constant diffusivity. This eliminates the effect of diffusivity enhancement. For comparison purposes, we assumed the same bulk diffusivity for both the Xe and vacancies. Clustering and re-solution only slightly reduced the bubble growth rate as compared to what a MOOSE-only simulation would predict. The coupled approach used here captures more realistic behavior. It has been reported that, at lower temperatures, re-solution releases more Xe monomers that are usually trapped within grains for typical grain sizes [11]. However, in the HBS regions, the smaller grain sizes and higher fraction of GB networks cause these new Xe monomers to make their way to the GBs and existing bubbles faster, causing the bubbles to grow. This behavior is also exacerbated by the enhanced diffusion behavior in the HBS region. Thus, the effect of clustering is minimized in this case. This supports the experimental observation of Xe depletion within the grain and the formation of large bubbles in HBS regions. Figure 2.12 shows the Xe source term and concentration of Xe monomers within the grain interior at an intermediate evolution stage. It is evident from these microstructural images that the intra-granular Xe concentration reduces with increased grain size. This supports the enhanced re-solution effect observed in HBS conditions.

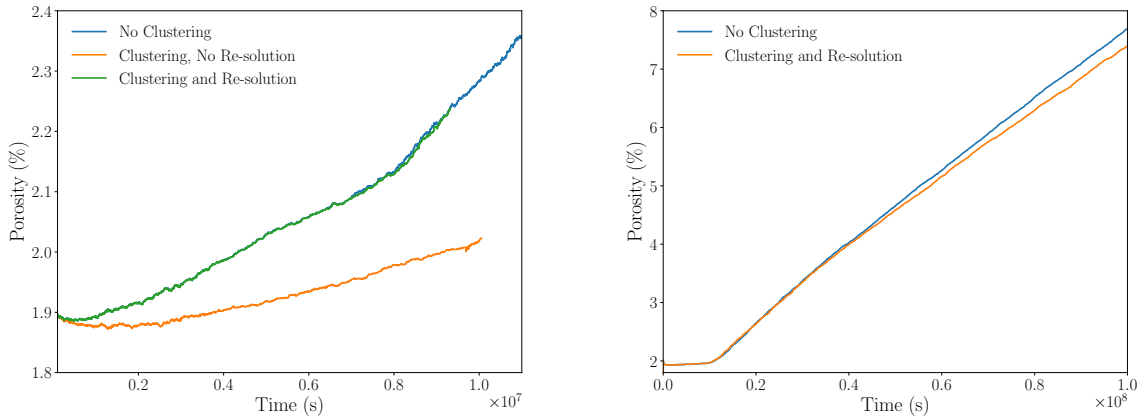

(a) (b)

Figure 2.11. Effect of intragranular mechanisms on intergranular bubble evolution with (a) enhanced diffusion and (b) constant diffusion.

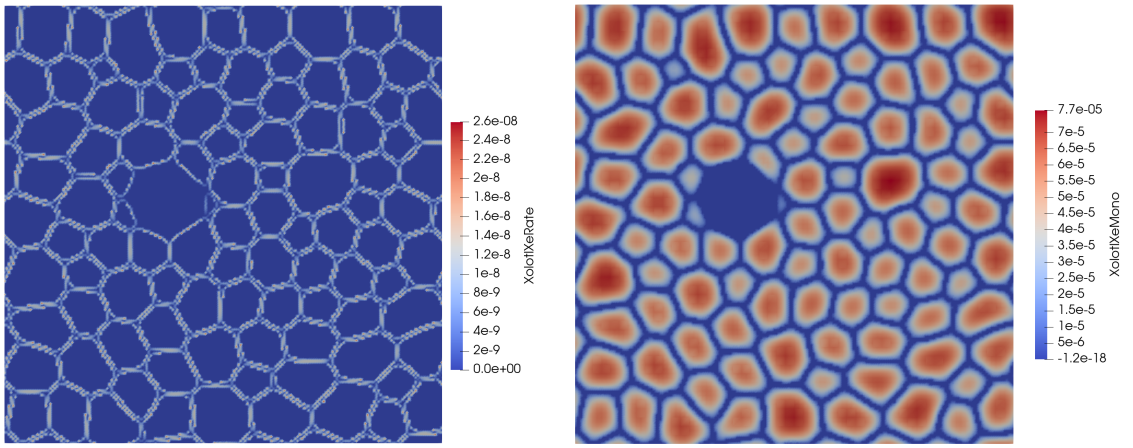

(a) (b)

Figure 2.12. a) Xe monomers arriving at the GBs from the Xolotl cluster dynamics simulations. (b) The concentration of Xe monomers within grain interiors.

2.2.2.4 Effect of the vacancy source term

The vacancy production rate under irradiation conditions is unknown. In a phase-field model, the effective vacancy production rate is generally calculated based on the steady-state vacancy concentration within the grains. White [27] showed that the defect production rate varies from 10,000 to 500,000 defects/fission. However, most of the vacancies produced are annihilated due to recombination and clustering with other defects and fission products. The current model does not track the interstitials and cannot consider defect interaction. Hence, the coupled model assumes the vacancy source term to be proportional to the Xe source term. Previously, a factor of 4 was used to estimate the vacancy source term in the phase-field model. This indicates that each Xe would bring an additional four vacancies. While this is valid for higher temperatures, for HBS conditions, the interaction between vacancies and interstitials could limit the number of vacancies that enter the existing bubbles. as shown through the 1-D analysis presented in Section 2.1.3. The effective vacancy source term derived from this analysis has been used in the following simulations. This captures the essence of the recombination of vacancies and interstitials and helps maintain the steady-state vacancy concentration in the matrix. Figure 2.13 presents the effect of the vacancy source term on the growth of existing bubbles. A steady growth of the existing bubble at a slower rate is observed with the current model.

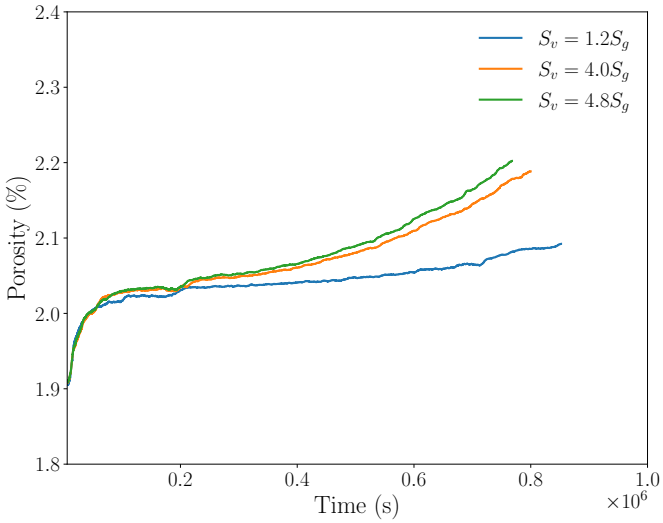

Figure 2.13. Effect of vacancy source term on porosity evolution over time.

2.3 Bubble pressure calculation

We now present the bubble evolution and corresponding pressure changes over time for different initial bubble sizes and temperatures. The bubble pressure is calculated using the van der Waals equation of system (Eq. 2.39). Figure 2.14 shows the bubble evolution for the initial 100, 150, and 200 nm bubbles at approximately $9{\times}10^5$ sec. The final bubble sizes reached for each of these cases were 105, 160, and 220 nm, respectively, and the corresponding bubble pressures reached were 219.5, 103.5, and 59.1 MPa, respectively. It is also worth noting here that the hybrid phase-field-cluster-dynamics model used this year resolves the numerical issues faced by these simulations prior to [7], and limits the formation of spontaneous intra-granular bubbles. These simulations can now capture the microstructural evolution of HBS over longer periods of time. The coupled approach also eliminates the possibility of a sudden pressure spike in the bubbles, due to numerical instabilities.

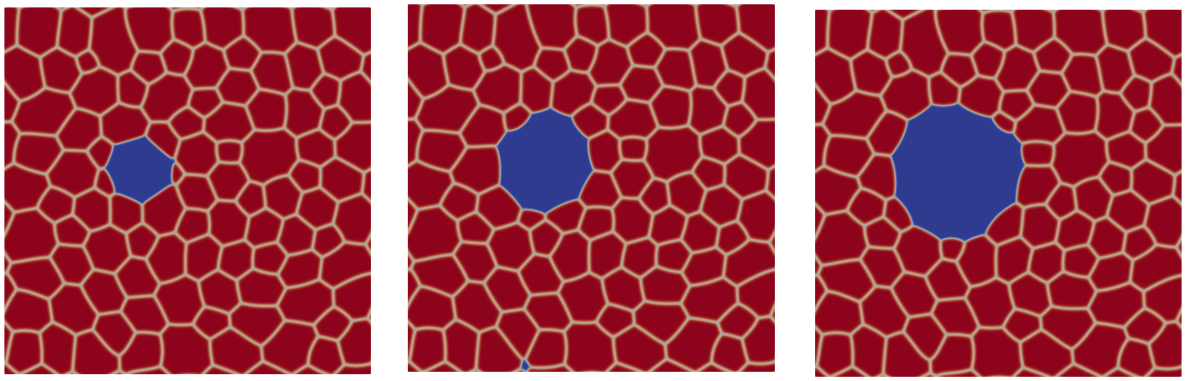

(a) (b) (c)

Figure 2.14. Bubble evolution in HBS at time approximately 9×10^5 seconds for the initial bubble radii of (a) 100, (b) 150, and (c) 200 nm.

Figure 2.15 shows the evolution of the 100 nm bubble at 1000, 1100, and 1200 K. The bubble growth rate decreases with decreased temperature. Hence, it takes longer for the same bubble to reach a certain size at lower temperatures. For all these cases, the bubble reached approximately 105 nm in size. For the same bubble, the pressures reached at 1200, 1100, and 1000 K are 220, 172, and 120 MPa, respectively.

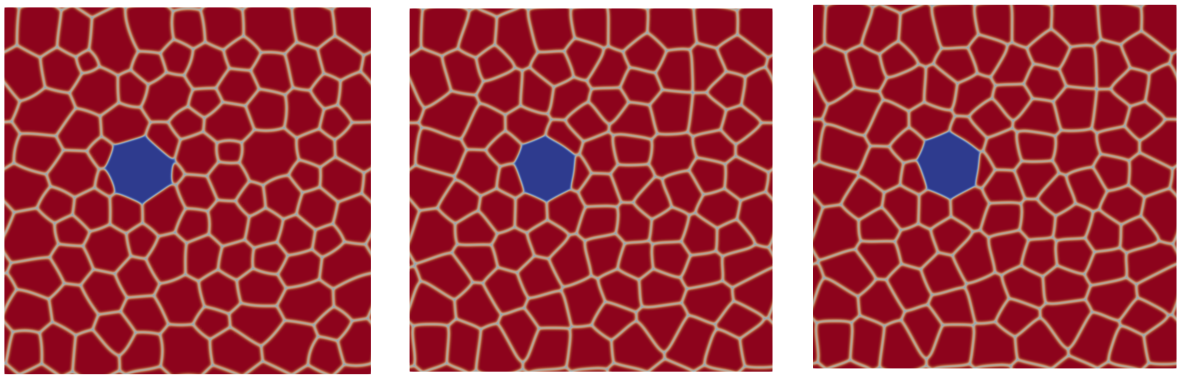

(a) (b) (c)

Figure 2.15. Evolution of an initial 100 nm bubble at (a) 1200, (b) 1100, and (c) 1000 K.

Figure 2.16a captures the porosity evolution over time for different initial bubble sizes, and Figure 2.16b compares the growth rate of a 100 nm bubble at 1200, 1100, and 1000 K. The bubble growth rate was observed to decrease with increased initial bubble size. The bubble growth rate also decreased with decreased temperature. Reductions in Xe and vacancy diffusivity with temperature hinder the bubble growth rate at lower temperatures.

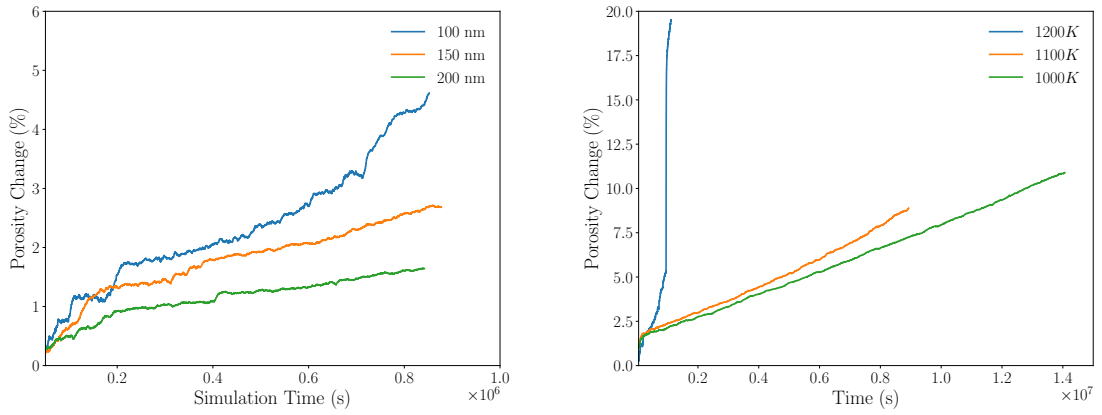

(a) (b)

Figure 2.16. Porosity evolution over time: (a) for different initial bubbles at 1200 K, and (b) for a 100 nm initial bubble at different temperatures.

Figure 2.17a shows the bubble pressure evolution over time for different initial bubble sizes, and Figure 2.17b depicts the pressure evolution of the 100 nm bubble at 1200, 1100, and 1000 K. The bubble pressure increased initially, then stabilized over time as the bubbles receive a constant flux of vacancies. The maximum pressures experienced by the 100, 150, and 200 nm bubbles at 1200 K were 213.4, 103.4, and 78.1 MPa, respectively.

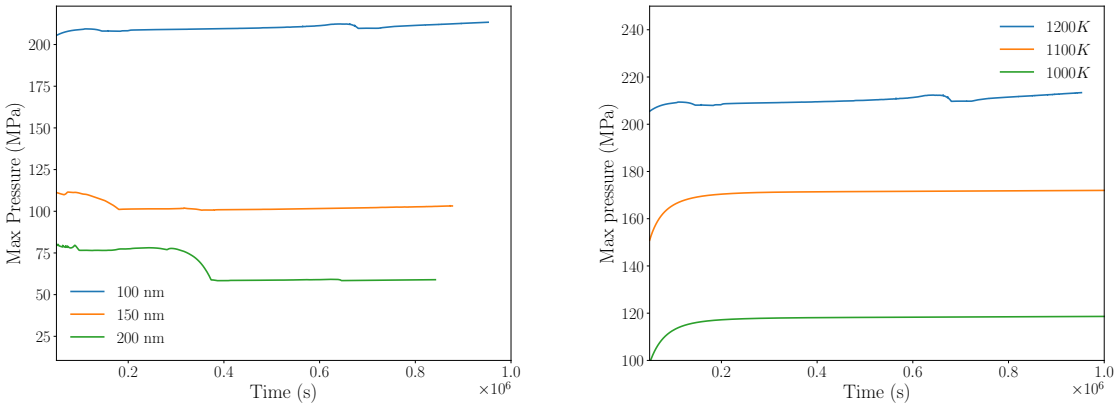

(a) (b)

Figure 2.17. Evolution of maximum bubble pressure over time: (a) for different initial bubbles at 1200 K, and (b) for a 100 nm initial bubble at different temperatures.

Figure 2.18 compares the bubble pressures calculated from these simulations to the analytical values obtained using

the dislocation punching criteria. The analytical value was calculated as:

$$P = P_{eq} + P_{ext} = P_h + \frac{2\gamma_{st}}{r} + \frac{Gb}{r}, \tag{2.45}$$

where P_{eq} is the equilibrium pressure and P_{ext} is the external pressure. γ_{st} is the surface tension, r is the bubble radius, G is the shear modulus, and b is the Burgers vector. The analytical pressure values were obtained from Eq. 2.45 by assuming the hydrostratic pressure to be zero. The pressure values obtained from the simulations were lower than the analytical values. Additionally, Figure 2.18b demonstrates that the pressure reached same-sized bubbles at different temperatures could be very different. This indicates that factors other than bubble radius contribute to increased bubble pressure. The defect concentration within the bubble is the primary driving factor in this regard. Bubble pressure also varies linearly with temperature. Thus, the analytical expression fails to capture different factors that could influence over-pressurization of the bubbles. In all the cases considered here, the pressures calculated from the mesoscale simulations are lower than the analytical values, meaning that engineering-scale models can still utilize the analytical values so as to remain conservative. In the future, a mesoscale-informed pressure evolution will be implemented in the engineering-scale model. It is also important to model the bubble evolution in 3-D in order to appropriately capture the bubble geometry. Moreover, the current model does not consider the surface tension effect on bubble growth and pressure evolution. This will be added in the future as well.

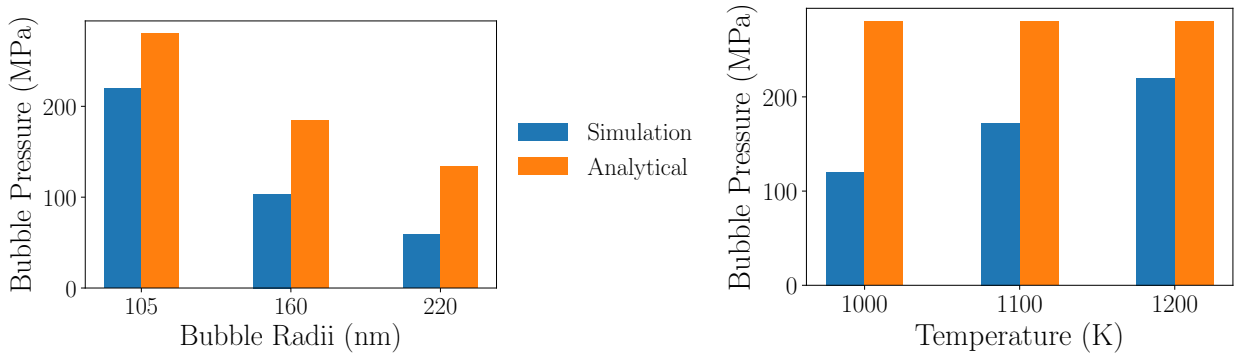

Figure 2.18. Bubble pressure calculated from the simulations and compared against the dislocation punching criteria: (a) for different initial bubbles at 1200 K, and (b) for a 100 nm initial bubble at different temperatures.

3. PHASE-FIELD FRACTURE MODELING OF UO_2 HBS PULVERIZATION

3.1 Phase-field fracture model

The phase-field fracture model is formulated based on the mechanics minimization problem that is regularized and approximated using the phase-field variable c, as per:

$$\{\boldsymbol{u}, c\} = \arg\min_{\boldsymbol{u},c} \Psi(\boldsymbol{u}, \boldsymbol{\nabla u}, c, \boldsymbol{\nabla} c), \tag{3.1a}$$

$$\text{subject to} \qquad \boldsymbol{u} = \boldsymbol{g}, \quad \forall \boldsymbol{x} \in \partial\Omega_D, \tag{3.1b}$$

$$\dot{c} \geqslant 0, \quad \forall \boldsymbol{x} \in \Omega, \tag{3.1c}$$

where u is the displacement vector. Eq. (3.1c) represents the irreversibility condition equivalent to the "no healing" condition on the permanent crack set. The objective function $\Psi(\boldsymbol{u}, \boldsymbol{\nabla u}, c, \boldsymbol{\nabla} c)$ is defined as:

$$\begin{aligned}\Psi(\boldsymbol{u}, \boldsymbol{\nabla u}, c, \boldsymbol{\nabla} c) =& \Psi_{\text{elastic}}(\boldsymbol{\nabla u}, g(c)) + \Psi^{l}_{\text{fracture}}(c, \boldsymbol{\nabla} c) - \Psi_{\text{dissipation}}(c) \\ &- \Psi^{\text{traction}}_{\text{external}}(\boldsymbol{u}) - \widetilde{\Psi}^{\text{pressure}}_{\text{external}}(\boldsymbol{u}, c, \boldsymbol{\nabla} c),\end{aligned} \tag{3.2a}$$

$$\Psi_{\text{elastic}}(\boldsymbol{\nabla u}, g(c)) = \int_{\Omega} g(c)\psi^{\langle \text{A} \rangle}_{\text{elastic}}(\boldsymbol{\nabla u})\, \mathrm{d}V + \int_{\Omega} \psi^{\langle \text{I} \rangle}_{\text{elastic}}(\boldsymbol{\nabla u})\, \mathrm{d}V, \tag{3.2b}$$

$$\Psi^{l}_{\text{fracture}}(c, \boldsymbol{\nabla} c) = \int_{\Omega} \mathcal{G}_c \gamma_l(c, \boldsymbol{\nabla} c)\, \mathrm{d}V, \tag{3.2c}$$

$$\dot{\Psi}_{\text{dissipation}}(\dot{c}) = \int_{\Omega} \frac{1}{2}\eta \dot{c}^2\, \mathrm{d}V, \tag{3.2d}$$

$$\Psi^{\text{traction}}_{\text{external}}(\boldsymbol{u}) = \int_{\partial\Omega_N} \boldsymbol{\tau} \cdot \boldsymbol{u}\, \mathrm{d}A, \tag{3.2e}$$

$$\widetilde{\Psi}^{\text{pressure}}_{\text{external}}(\boldsymbol{u}, c, \boldsymbol{\nabla} c) = -\int_{\Omega} p \boldsymbol{\nabla} c \cdot \boldsymbol{u} I'(c)\, \mathrm{d}V. \tag{3.2f}$$

It considers the energy contribution due to deformation (Ψ_{elastic}), fracture ($\Psi^{l}_{\text{fracture}}$, internal dissipation ($\Psi_{\text{dissipation}}$), and external pressure ($\Psi^{\text{traction}}_{\text{external}}$, $\widetilde{\Psi}^{\text{pressure}}_{\text{external}}$). Let us define the trial spaces:

$$\mathcal{U} = \left\{ \boldsymbol{u} | \boldsymbol{u} \in \mathcal{H}^1(\Omega)^d, \boldsymbol{u} = \boldsymbol{g}, \forall \boldsymbol{x} \in \partial\Omega \right\}, \quad \mathcal{C} = \left\{ c | c \in \mathcal{H}^1(\Omega), \dot{c} \geqslant 0, \forall \boldsymbol{x} \in \Omega \right\}, \tag{3.3}$$

along with their corresponding weighting spaces:

$$\mathcal{V} = \left\{ \delta\boldsymbol{u} | \delta\boldsymbol{u} \in \mathcal{H}^1(\Omega)^d, \boldsymbol{u} = \boldsymbol{0}, \forall \boldsymbol{x} \in \partial\Omega \right\}, \quad \mathcal{Q} = \left\{ \delta c | \delta c \in \mathcal{H}^1(\Omega), \delta c \geqslant 0, \forall \boldsymbol{x} \in \Omega \right\}. \tag{3.4}$$

The optimality conditions for $\boldsymbol{u}$ follow from the functional derivative of the objective function Ψ, as per:

$$\begin{aligned} &\int_{\Omega} \boldsymbol{\nabla} \cdot \frac{\partial \psi_{\text{elastic}}(\boldsymbol{\nabla u}, g(c))}{\partial \boldsymbol{\nabla u}} \, \mathrm{d}V - \int_{\partial\Omega_N} \frac{\partial \psi_{\text{elastic}}(\boldsymbol{\nabla u}, g(c))}{\partial \boldsymbol{\nabla u}} \boldsymbol{n} \, \mathrm{d}A \\ &+ \int_{\partial\Omega_N} \frac{\partial \psi^{\text{traction}}_{\text{external}}(\boldsymbol{u})}{\partial \boldsymbol{u}} \, \mathrm{d}A + \int_{\Omega} \frac{\partial \widetilde{\psi}^{\text{pressure}}_{\text{external}}(\boldsymbol{u}, c, \boldsymbol{\nabla} c)}{\partial \boldsymbol{u}} \, \mathrm{d}V = 0, \quad \forall \Omega' \subseteq \Omega, \forall \partial\Omega'_N \subseteq \partial\Omega_N. \end{aligned} \tag{3.5}$$

Substituting (3.2) yields:

$$\boldsymbol{\nabla} \cdot \boldsymbol{\sigma} - pI'(c)\boldsymbol{\nabla} c = \boldsymbol{0}, \quad \forall \boldsymbol{x} \in \Omega, \tag{3.6a}$$

$$\boldsymbol{\sigma n} = \boldsymbol{\tau}, \quad \forall \boldsymbol{x} \in \Omega_N, \tag{3.6b}$$

where $\boldsymbol{\sigma} = \dfrac{\partial \psi_{\text{elastic}}}{\partial \boldsymbol{\nabla u}}$ is the stress-strain constitutive relation. The optimality conditions for c that are subject to the irreversibility constraint (3.1c) also follow from the functional derivative (with respect to the rate of the objective function) and recover the Karush–Kuhn–Tucker conditions, such that:

$$\begin{aligned} &\int_{\Omega} \frac{\partial \psi_{\text{elastic}}(\boldsymbol{\nabla u}, g(c))}{\partial c} \dot{c} \, \mathrm{d}V - \int_{\Omega} \boldsymbol{\nabla} \cdot \frac{\partial \psi^{l}_{\text{fracture}}(c, \boldsymbol{\nabla} c)}{\partial \boldsymbol{\nabla} c} \dot{c} \, \mathrm{d}V + \int_{\partial\Omega} \frac{\partial \psi^{l}_{\text{fracture}}(c, \boldsymbol{\nabla} c)}{\partial \boldsymbol{\nabla} c} \cdot \boldsymbol{n} \dot{c} \, \mathrm{d}A \\ &+ \int_{\Omega} \frac{\partial \psi^{l}_{\text{fracture}}(c, \boldsymbol{\nabla} c)}{\partial c} \dot{c} \, \mathrm{d}V + \int_{\Omega} \boldsymbol{\nabla} \cdot \frac{\partial \widetilde{\psi}^{\text{pressure}}_{\text{external}}(c, \boldsymbol{\nabla} c)}{\partial \boldsymbol{\nabla} c} \dot{c} \, \mathrm{d}V - \int_{\partial\Omega} \frac{\partial \widetilde{\psi}^{\text{pressure}}_{\text{external}}(c, \boldsymbol{\nabla} c)}{\partial \boldsymbol{\nabla} c} \cdot \boldsymbol{n} \dot{c} \, \mathrm{d}A \\ &+ \int_{\Omega} \frac{\partial \widetilde{\psi}^{\text{pressure}}_{\text{external}}(c, \boldsymbol{\nabla} c)}{\partial c} \dot{c} \, \mathrm{d}V + \int_{\Omega} \frac{\partial \dot{\psi}_{\text{dissipation}}(\dot{c})}{\partial \dot{c}} \dot{c} \, \mathrm{d}V = 0, \quad \forall \Omega' \subseteq \Omega, \forall \partial\Omega'_N \subseteq \partial\Omega_N. \end{aligned} \tag{3.7}$$

Again, substituting (3.2) yields:

$$\begin{aligned} &\phi^f \geqslant 0, \quad \dot{c} \geqslant 0, \quad \phi^f \dot{c} = 0, \\ &\text{with } \phi^f = \begin{cases} \eta\dot{c} - \boldsymbol{\nabla} \cdot \boldsymbol{\xi} + \dfrac{\mathcal{G}_c}{c_0 l} \alpha'(c) - Y, & \forall \boldsymbol{x} \in \Omega, \\ \boldsymbol{\xi} \cdot \boldsymbol{n} + pI'(c)\boldsymbol{u} \cdot \boldsymbol{n}, & \forall \boldsymbol{x} \in \partial\Omega \end{cases}, \end{aligned} \tag{3.8}$$

where $\boldsymbol{\xi} = \dfrac{\partial \psi^{l}_{\text{fracture}}}{\partial \boldsymbol{\nabla} c} = \dfrac{2\mathcal{G}_c l}{c_0}\boldsymbol{\nabla} c$ is the thermodynamic conjugate to $\boldsymbol{\nabla} c$, and Y is the generalized fracture driving force consisting of contributions from the active elastic energy density as well as work done by pressure:

$$Y = -g'(c)\psi^{\langle \mathrm{A} \rangle}_{\text{elastic}} + pI'(c)\boldsymbol{\nabla} \cdot \boldsymbol{u}. \tag{3.9}$$

With a view toward the solution strategy, using a variational inequality solver (e.g., a primal-dual active set algorithm) to enforce the irreversibility constraint requires discretization of the fracture envelope ϕ^f only on the inactive sets $\dot{c} > 0$ and $\phi^f = 0$. Hence, only the weak form in the case of $\phi^f = 0$ is outlined below:

Given $\boldsymbol{g}$, $\boldsymbol{\tau}$, and c_0, find $\boldsymbol{u} \in \mathcal{U}$ and $c \in \mathcal{C}$, such that $\forall \delta \boldsymbol{u} \in \mathcal{V}$ and $\forall \delta c \in \mathcal{Q}$:

$$\int_{\Omega} \boldsymbol{\sigma} : \boldsymbol{\nabla} \delta \boldsymbol{u} \, \mathrm{d}V + \int_{\Omega} pI'(c)\boldsymbol{\nabla} c \cdot \delta \boldsymbol{u} \, \mathrm{d}V - \int_{\partial \Omega_N} \boldsymbol{\tau} \cdot \delta \boldsymbol{u} \, \mathrm{d}A = 0, \tag{3.10a}$$

$$\int_{\Omega} \eta \dot{c} \delta c \, \mathrm{d}V + \int_{\Omega} \boldsymbol{\xi} \cdot \boldsymbol{\nabla} \delta c \, \mathrm{d}V + \int_{\Omega} \frac{\mathcal{G}_c}{c_0 l} \alpha'(c) \delta c \, \mathrm{d}V - \int_{\Omega} Y \delta c \, \mathrm{d}V + \int_{\partial \Omega} pI'(c) \boldsymbol{u} \cdot \boldsymbol{n} \delta c \, \mathrm{d}A = 0. \tag{3.10b}$$

Furthermore, the macro-scale pulverization behavior is approximated by using periodic boundary conditions (PBCs). PBCs are useful for avoiding the boundary effects caused by finite size, and for making the system deform like an infinite one. In MOOSE, the global strain system was implemented to enforce the PBC [28]. The global strain system can capture the deformation with applied loads while still maintaining the periodic strains.

3.2 Model simplifications for 3-D analysis

This year's primary focus is on using 3-D phase-field fracture simulations to obtain the updated critical pressure value for the pulverization criteria. To this end, several simplifications were made to the model in order to reduce the computational cost associated with large 3-D simulations. First of all, for the 3-D simulations, the GBs are not explicitly modeled. The 3-D simulations also used $distributedmesh$ to limit the memory usage. Figure 3.1 compares the ideal 3-D microstructure against the simplified geometry used in the 3-D analysis.

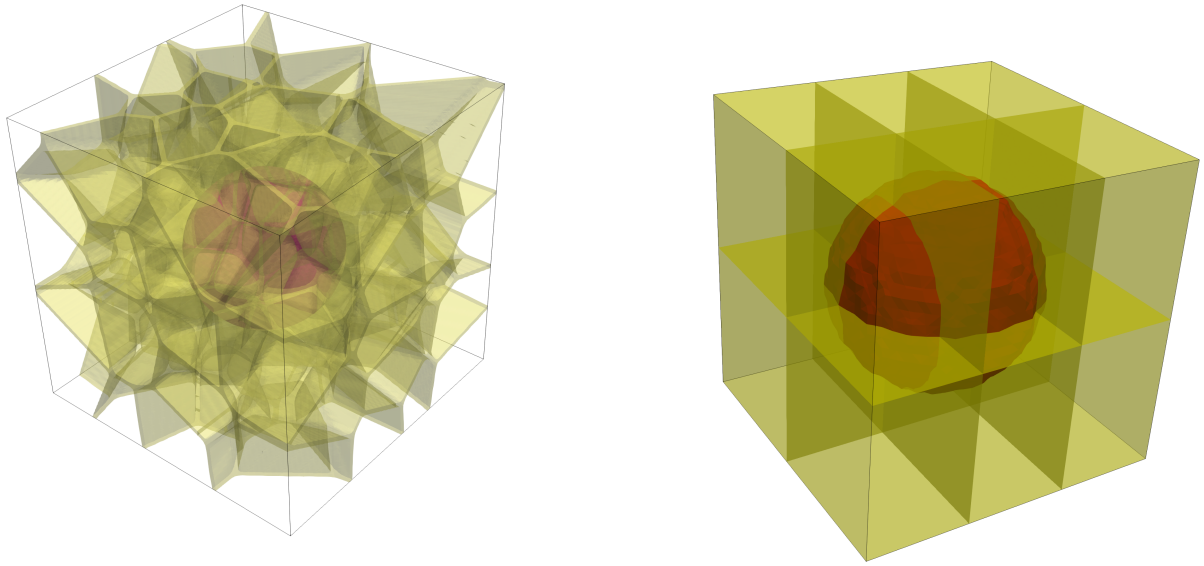

(a) (b)

Figure 3.1. (a) Ideal 3-D microstructure with grains. (b) Simplified 3-D geometry considered for fracture simulations (internal mesh partition surfaces for the distributed mesh are shown). The bubble radius considered was 500 nm.

To study the impact of the simplification on the fracture behavior, a 2-D simulation with 0.162 porosity and no external pressure was analyzed. The energy release rate of the matrix was set to a uniform value representing the GB's energy release rate of 0.0012 Pa.m, the value considered in last year's simulations. Figure 3.2 compares the crack pattern observed in the ideal 2-D HBS structure with the crack path obtained from the simplified geometry. It was observed that, due to PBCs, the crack locations are symmetric in both cases. Moreover, irrespective of whether the GBs are explicitly modeled, the critical pressure obtained in both simulations was 104 MPa. Although the GB network could influence the crack propagation path, side branching, and fragmentation sizes, these values are not taken into account when determining the pulverization criteria. Pulverization occurs when the bubble pressure exceeds the critical value. In this case, the critical pressure was determined based on the crack initiation rather than the crack propagation leading to fragmentation, and the critical pressure remained unchanged with respect to the geometric simplifications made here. Thus, the geometric simplifications made here do not influence the determination of the pulverization criteria.

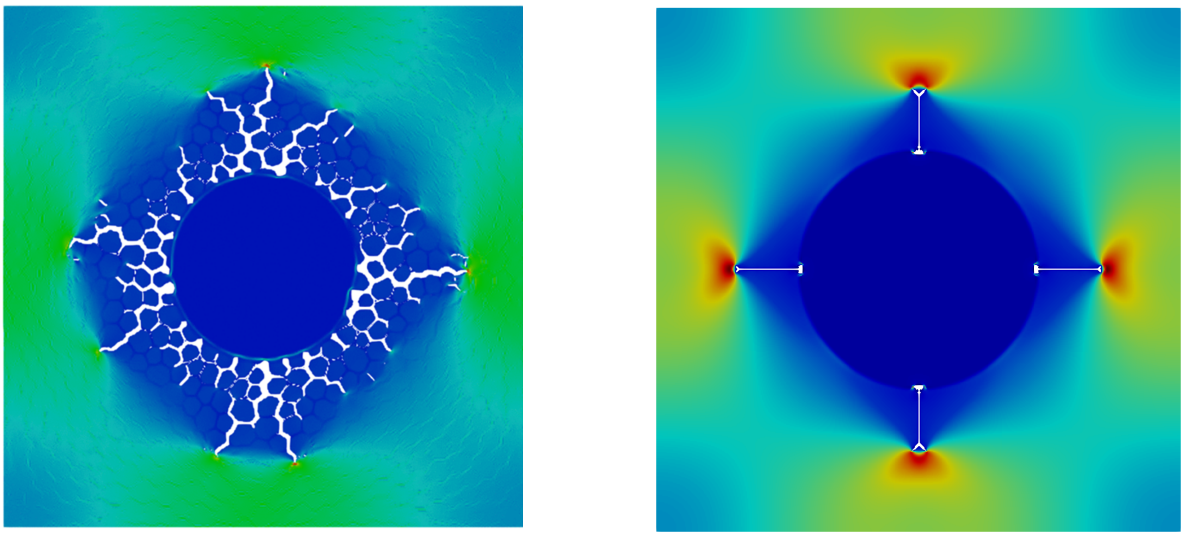

(a) (b)

Figure 3.2. (a) Crack pattern in the ideal 2-D HBS structure [7], and (b) crack growth captured by the simplified geometry without grains. In both cases, the crack pattern is symmetric, and crack initiation occurs at the critical bubble pressure of 104 MPa. Thus, the geometric simplifications made here do not influence the determination of the pulverization criteria.

Additionally, to further reduce the computational cost, larger element sizes were used in the 3-D simulations. Figure 3.3 depicts the critical pressures calculated from the aforementioned 2-D simulation with varying element sizes, along with the error in the calculation. The maximum error observed for the coarsest configuration was approximately 1%. Although the large element sizes will not be able to appropriately resolve the length scale for crack propagation, the critical pressure for crack initiation can be accurately predicted. Based on this analysis, an element size of 0.05 was determined sufficient for use in the 3-D simulations. This limits the computational cost while correctly determining the pulverization criteria in 3-D.

3.3 Determination of the pulverization criteria

To inform development of the updated Bison model, several simulations with varying porosity, critical stress, and external pressure were performed. The porosity was defined as $p = \frac{4}{3}\pi r^3/(l)^3$, where r is the bubble size of 0.5 μm and l is the domain length. The domain length was varied from 1.5 to 2.0 μm to obtain different porosity levels. Additionally, the external compressive loads of 0, 30, and 60 MPa were applied uniformly on the domain. Due to uncertainty in determining the critical fracture stress for high-burnup UO_2 from macroscale data on porous samples, three critical fracture stresses (i.e., 130, 160, and 200 MPa) were considered. The pressure inside a bubble places a circumferential tensile stress in the matrix. When this tensile stress reaches critical fracture strength, cracks initiate at the bubble/matrix interface. The critical pressure values extracted from all the simulations are provided in Tables 3.1, 3.2, and 3.3 for a

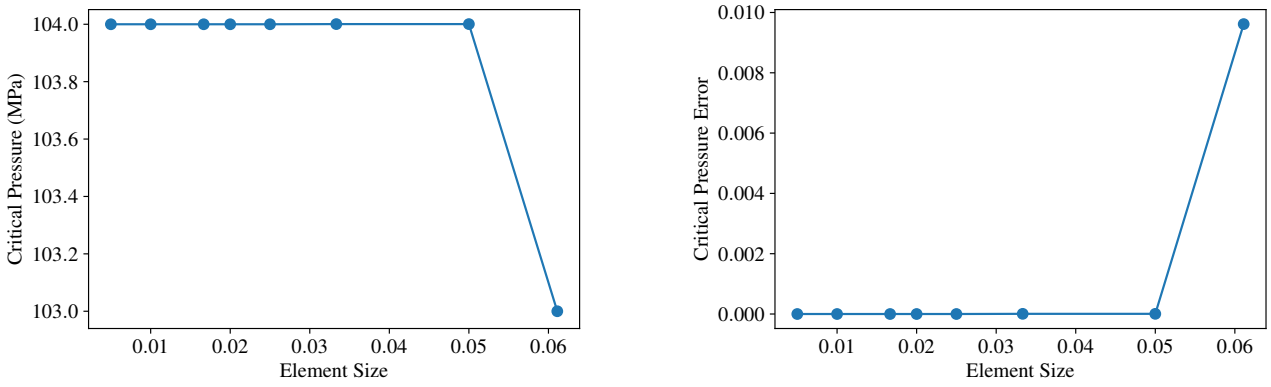

Figure 3.3. Convergence analysis for critical pressure calculation: (a) variation of critical pressure, and (b) error in the critical pressure calculation with element size.

critical stress of 130, 160, and 200 MPa, respectively. For all the cases considered, the critical pressures obtained from the 3-D simulation exceed the values previously calculated from corresponding 2-D simulations. This indicates that 2-D simulations are conservative in predicting the critical pressure for pulverization. 3-D simulations capture more realistic behavior, as the bubble geometry is captured accurately and the stresses are calculated appropriately, without simplifications being made to the out-of-plane components. More rigorous 3-D analysis with grain structure will be performed in the future.

Porosity / P_{ext}(MPa)	0.155	0.128	0.107	0.09	0.062
0	132	140	144	152	156
30	164	176	180	184	189
60	200	208	216	220	220

Table 3.1. Critical pressure values for $\sigma_{cr} = 130$ MPa.

Porosity / P_{ext}(MPa)	0.155	0.128	0.107	0.09	0.062
0	144	152	156	164	168
30	176	180.5	192	196	200
60	208	20	228	232	236

Table 3.2. Critical pressure values for $\sigma_{cr} = 160$ MPa.

Porosity / P_{ext}(MPa)	0.155	0.128	0.107	0.09	0.062
0	160	172	180	184	192
30	192	200	208	216	176
60	220	232	240	244	252

Table 3.3. Critical pressure values for $\sigma_{cr} = 200$ MPa.

4. IMPROVEMENTS TO THE BISON UO_2 HBS PULVERIZATION CRITERION

The initial development of the Bison pulverization criterion for high-burnup UO_2 was described in Ref. [7]. The model was implemented in the Bison material property `UO2PulverizationMesoscale`, and tracks the average pressure of bubbles P_g in regions where the HBS has formed. When the volume fraction of the HBS phase exceeds the threshold value (50% by default, although this parameter can be adjusted by the user), it is assumed that pulverization can occur. In these regions, P_g is compared to the critical pressure necessary for pulverization to occur, P_g^{cr}, and if $P_g > P_g^{cr}$, pulverization occurs and the material property `pulverized` changes from 0 to 1.

In this year's work, several improvements were made to the pulverization criterion. Previously, the P_g and bubble sizes were assumed to be constant, but this did not account for the additional gas atoms due to Xe production, or the bubble growth due to vacancy flux, which is expected to occur because the bubbles in the HBS region are believed to be over-pressurized relative to equilibrium. Section 4.1 describes the modifications made to the Bison model to account for bubble growth and pressure changes due to these effects. Section 4.2 describes the modifications to the value of P_g^{cr}, based on the phase-field fracture simulations covered in Section 3.

4.1 Evolution equation for bubble pressure in the HBS region

In the original Bison UO_2 pulverization model, the initial pressure of the bubbles in the HBS region was assumed to be 100 MPa at a temperature of 400°C, based on the dislocation punching criterion surrounding bubbles in the HBS region [29]. Phase-field simulations of the HBS formation process in the previous FY milestone showed dislocation punching pressure to be a reasonable estimate of the initial bubble pressure [7]. The initial average bubble radius was assumed to be 0.53 μm [30]. However, the bubble pressure and radius were assumed to be static in the previous model; temperature was the only factor that affected pressure. This neglects the effects of additional gas atoms produced by fission diffusing to the existing bubbles, and also neglects the transport of vacancies and subsequent bubble growth, as driven by the over-pressurization of the HBS bubbles.

To evolve the bubble pressure and radius as a function of time, an approach similar to that used for the evolution of intra-granular bubbles in U_3Si_2 [31] was employed, with simplifications made to the treatment of gas atoms. The volume fraction of HBS in each quadrature point was tracked with the Bison material property `HighBurnupStructureFormation`. The initial bubble radius, volume, and pressure are set when the volume fraction of HBS in a given quadrature point

exceeds the threshold value of 50%. The initial bubble radius $R_b = 0.53$ μm, bubble volume $V_b = \frac{4}{3}\pi R_b^3$, and pressure $P = 100$ MPa. The number of bubbles per unit volume, $N = 2 \times 10^{17}$ m^{-3} [31], is assumed to be constant in time. The change in bubble volume with time is calculated as follows [31]:

$$\frac{dV_b}{dt} = \omega \frac{d\bar{n}}{dt} + \Omega \frac{dn_{iv}}{dt}, \tag{4.1}$$

where $\omega = 8.5 \times 10^{-29}$ m^3 is the van der Waals atomic volume for Xe [32], $\bar{n}$ is the number of gas atoms per bubble, $\Omega = 4.09 \times 10^{-29}$ m^3 is the volume of a U lattice site in UO_2 [33], and n_{iv} is the number of vacancies per intra-granular bubble. The initial values of $\bar{n}$ and n_{iv} at the time of HBS formation can be found from a rearranged formulation of the van der Waals equation of state [31]:

$$P = \frac{kT}{\Omega} \frac{\bar{n}}{n_{iv}} \tag{4.2}$$

combined with the integral form of Equation 4.1:

$$V_b = \omega \bar{n} + \Omega n_{iv}. \tag{4.3}$$

Combining and rearranging, the following is obtained:

$$\bar{n} = \frac{V_b}{\omega + \frac{kT}{P}}. \tag{4.4}$$

For the given initial conditions, $\bar{n} = 3.5 \times 10^9$. Using this, n_{iv} can be calculated:

$$n_{iv} = \frac{V_b - \omega \bar{n}}{\Omega}, \tag{4.5}$$

which results in $n_{iv} = 7.97 \times 10^9$.

The bubble volume was calculated for each subsequent time step by applying Equation 4.3, using updated values of $\bar{n}$ and n_{iv}. To simplify the calculation of n_v, a quasi-steady state solution to the diffusion equation for gas atoms was assumed [32]. In this case, the number of gas atoms transported to each existing bubble was simply equal to the production rate per unit volume, divided by the number of bubbles per unit volume:

$$\frac{d\bar{n}}{dt} = \frac{Y\dot{F}}{N}, \tag{4.6}$$

where Y is the fission gas yield and $\dot{F}$ is the fission rate density. So that the existing function `BubbleRadius` from the Bison header `IntraGranularFissionGas.h` can be used, the change is calculated in terms of the total concentration of gas found in the bubbles per unit volume of fuel, m, given in mol/m^3:

$$m = \frac{\bar{n}N}{N_A}, \tag{4.7}$$

where N_A is Avogadro's number. Substituting Equation 4.6 into 4.7 produces:

$$\frac{dm}{dt} = \frac{d}{dt}\left(\frac{\bar{n}N}{N_A}\right) = \frac{N}{N_A}\frac{d\bar{n}}{dt} = \frac{N}{N_A}\frac{Y\dot{F}}{N} = \frac{Y\dot{F}}{N_A}. \tag{4.8}$$

An updated value for m was calculated in each time step and then passed into the `BubbleRadius` function. From this value, the updated value of $\bar{n}$ was calculated by rearranging Equation 4.7 for use in Equation 4.3. The updated value for n_{iv} was calculated as [31]:

$$\frac{dn_{iv}}{dt} = \frac{2\pi D_{ig}^{v}\rho}{kT\zeta}\left(P - P_{eq}\right), \tag{4.9}$$

where D_{ig}^{v} is the intra-granular vacancy diffusion coefficient, ρ is the radius of the equivalent Wigner-Seitz cell surrounding a bubble, and ζ is a dimensionless factor defined as:

$$\zeta = \frac{10\psi(1+\psi^3)}{-\psi^6 + 5\psi^2 - 9\psi + 5}, \tag{4.10}$$

where $\psi = R_b/\rho$. P_{eq} is the equilibrium pressure for a bubble of radius R_b, as calculated using the Laplace-Young equation:

$$P_{eq} = \frac{2\gamma}{R_b} - \sigma_h, \tag{4.11}$$

where $\gamma = 1$ J/m^2 [33] is the surface tension of the bubble-matrix interface and σ_h is the hydrostatic stress, considered to be negative for a solid in compression.

After updated values of $\bar{n}$ and n_{iv} were calculated using Equations 4.6 and 4.9, the updated bubble volume was calculated using Equation 4.3 in the `BubbleRadius` function, along with the corresponding bubble radius using:

$$R_b = \sqrt[3]{\frac{3V_b}{4\pi}}. \tag{4.12}$$

The updated bubble pressure was then calculated using Equation 4.2 for comparison with P_g^{cr}.

To test the behavior of the updated Bison model, the evolution of bubbles in the HBS region was simulated, with $t = 0$ being defined as the time at which complete HBS formation occurs, using constant parameters of $T = 673.15$ K, $\sigma_h = -10$ MPa, and $\dot{F} = 1 \times 10^{19}$ m^{-3}s^{-1}. The bubble pressure and radius as a function of time are shown in Figure 4.1. The bubbles are significantly over-pressurized at $t = 0$ ($P_{eq} = 13.8$ MPa using Equation 4.11). This over-pressurization leads to a strong driving force for vacancies, causing the bubble pressure to drop significantly and leading to the expected bubble growth.

4.2 Updated pulverization criterion based on 3-D phase-field fracture results

The BISON pulverization criterion was updated based on the bubble pressure obtained from the simplified 3-D phase-field fracture simulations. Here, the function for the critical bubble pressure is expressed as a function of porosity,

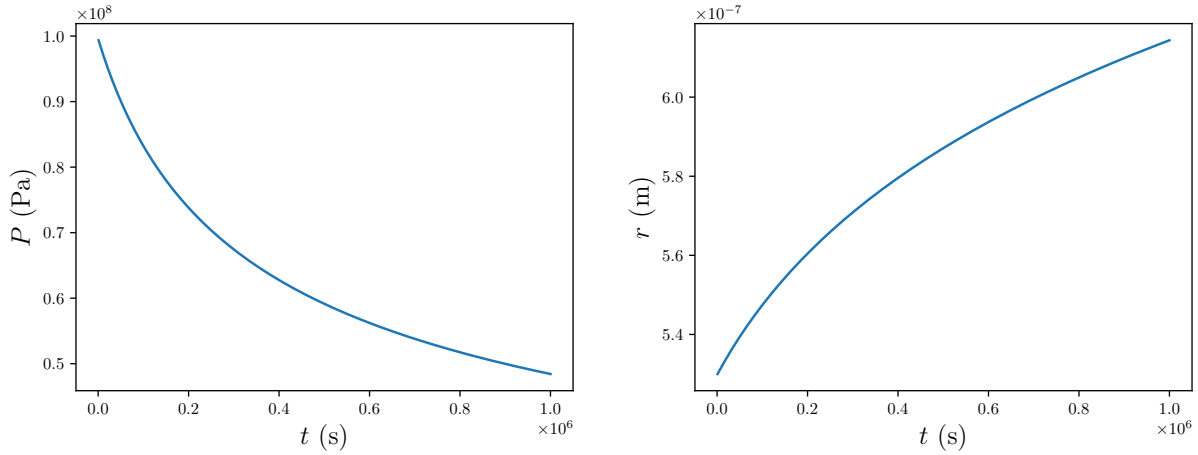

(a) (b)

Figure 4.1. (a) Pressure and (b) radius of bubbles in the HBS region. $t = 0$ is the time at which HBS formation occurs. The bubbles are significantly over-pressurized at $t = 0$, leading to a vacancy flux that decreases the bubble pressure and causes growth.

critical fracture stress, and applied external pressure, such that:

$$P_g^{cr} = [a + b\,(\sigma_{cr} - 130)](1 - c\,p) - d\,P_{ext}, \tag{4.13}$$

where σ_{cr}(MPa) is the critical fracture stress, p is the porosity, P_{ext}(MPa) is the external applied pressure, and a, b, c, and d are fitting coefficients. For the Bison the pulverization criterion, the values of a, b, c, and d were obtained by fitting the data of Section 3.3 using Python's `curve_fit` function. Thus, the fitted function of critical bubble pressure was:

$$P_g^{cr} = [175.987 + 0.5035(\sigma_{cr} - 130)](1 - 1.582p) + 1.089\,P_{ext}, \tag{4.14}$$

where pressures and stresses are provided in MPa. Comparisons of the fitted function and simulation data for a few select cases are shown in Figures 4.2 and 4.3. The coefficient values were updated from the previous year's model, which was derived from the 2-D calculations. A linear trend was observed for all the input parameters.

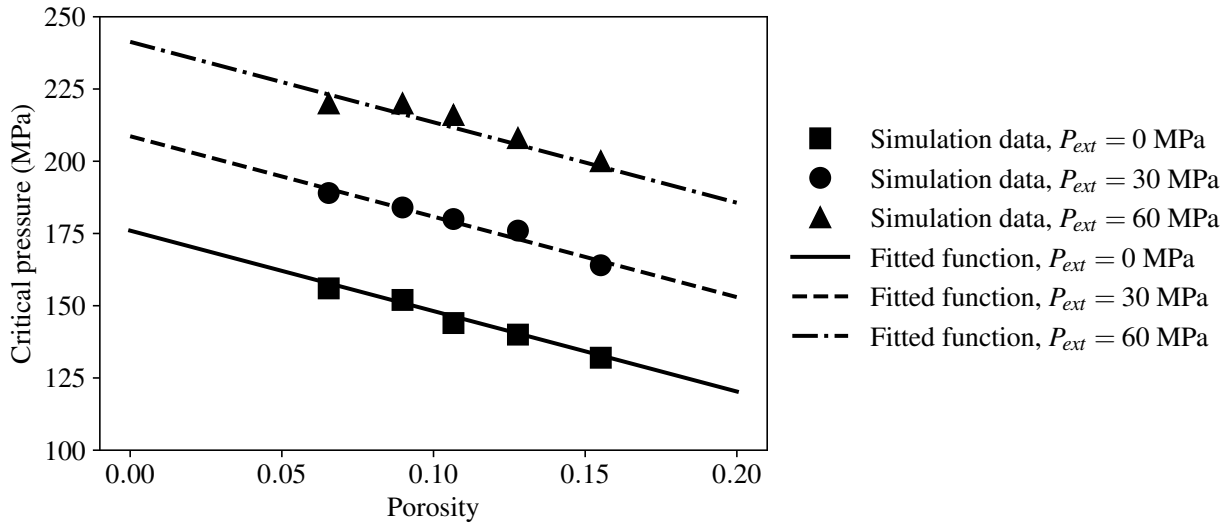

Figure 4.2. Comparison of the critical pressure obtained from the simulations for different external stresses with the fitted function (for critical fracture stress, $\sigma_{cr} = 130$ MPa).

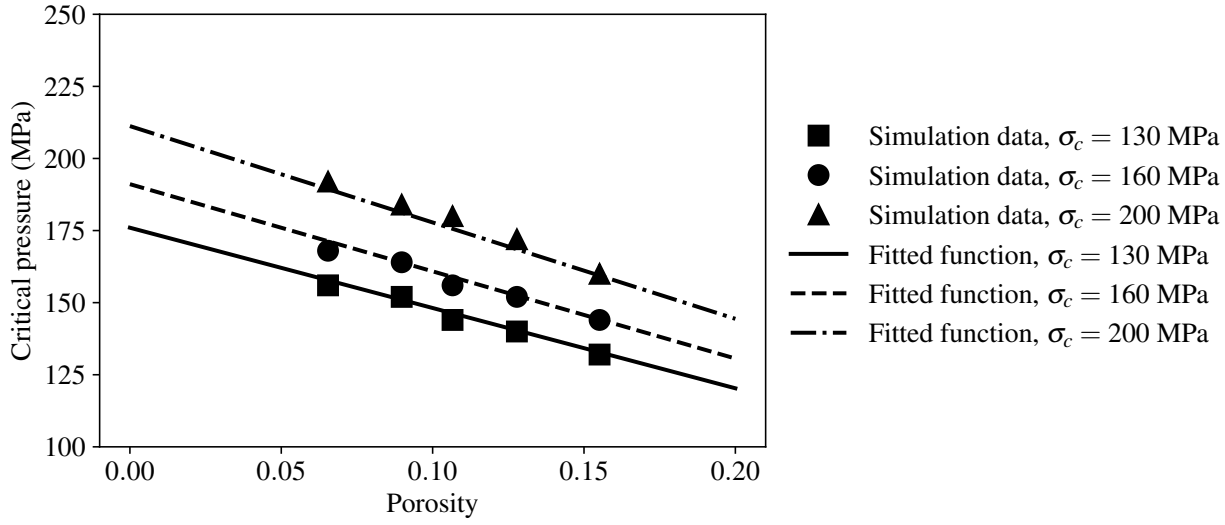

Figure 4.3. Comparison of the critical pressure obtained from the simulation for different critical fracture pressures with the fitted function (no external pressure).

4.3 Pore-pressurization-driven fracture coupled with smeared cracking models

In the pulverization criteria developed from 3-D phase-field simulations in Section 4.2 and expressed in a functional form in Equation 4.14, pulverization at a material point is influenced by bubble pressure, porosity, and externally applied pressure. Because they compute the quantities that are inputs to a pulverization model, engineering-scale fuel performance models are an essential component of mechanistic predictions of the extent of pulverization in a fuel rod under conditions of interest for safety analyses.

To calculate the externally applied stresses used by a pulverization criterion, a fuel performance model should account for the following:

1. Stresses caused by exposure of the fuel to reactor operating conditions over its normal lifetime. This should include the effects of thermal gradients, swelling, creep, plasticity, and fractures. These phenomena lead to large variations in the stresses in the radial, azimuthal and axial directions within a pellet.
2. Stresses caused by over-pressurization of fission gas bubbles due to elevated temperatures in a LOCA. These include both the local stresses from the material being placed in tension from over-pressurized pores and stresses induced in adjacent regions due to spatially non-uniform swelling.
3. Loss of the material's mechanical strength as it is pulverized.
4. Effects of HBS formation on material properties, including porosity, pore pressure, and mechanical properties.

A prior effort in support of a Electric Power Research Institute strategic partnership project [34] used a poromechanics-based approach to account for the effects of overpressurization on the stress state (Item 2 above). This was used within 2-D planar models of high-burnup light-water reactor fuel subjected to prototypical LOCA conditions in the Studsvik 191 and 196 rods. These simulations included a full set of models to account for the important aspects of nonlinear mechanical behavior (Item 1 above), and used a smeared cracking model to account for loss of strength due to pulverization and mechanically driven fracture (Item 3 above). Importantly, while this prior work did use an empirical model for HBS porosity, it did not account for the effects of HBS on pore pressure or mechanical properties (Item 4 above). Because the poromechanics approach captures the effects of pore pressure on the macroscopic stress, the smeared cracking model used to represent pulverization did account for pore pressure, but did not account for the effect of HBS on the strength of the material.

4.3.1 Poromechanics-based approach summary

The basic elements of the poromechanics-based approach are summarized here. In poromechanics theory, which is widely used in simulations of geological media that account for porous flow and mechanical deformation (e.g., [35, 36]), the standard Cauchy stress $\boldsymbol{\sigma}$ is replaced by an effective stress $\boldsymbol{\sigma}_{eff}$ in the mechanical equilibrium calculation, where the effective stress is defined as:

$$\boldsymbol{\sigma}_{eff} = \boldsymbol{\sigma} + pb\boldsymbol{I}, \tag{4.15}$$

where p is the pore pressure, b is the Biot coefficient (defined as the volumetric strain in a porous material subjected to a unit pore pressure), and $\boldsymbol{I}$ is the identity tensor. It is important to note that by accounting for the effect of pore

pressurization in this manner, application of pore pressure results in both volumetric expansion and a macroscopic tensile stress. This is in contrast to applying an eigenstrain, which results in volumetric expansion, but no stress in an unrestrained body.

To determine the appropriate Biot coefficient, a series of simulations were performed in [34], with varying porosity achieved by randomly deleting finite elements in a regular 3-D mesh of a cubic unit cell. From these simulations, the following relationship for the Biot coefficient as a function of HBS porosity was developed:

$$b = p_{hbs}(6.668p_{hbs} + 0.5761), \tag{4.16}$$

where p_{hbs} is the HBS porosity.

The Biot coefficient was also reduced to account for fracture, because fracture at a material point would provide an opportunity for pore-gas release, so pore pressurization should not affect fully damaged material. This was treated in an ad hoc fashion in the 2-D planar models employed by multiplying the Biot coefficient by a factor of $(1 - d_1 d_2)$, where d_1 and d_2 are the two in-plane components of the cracking damage index, which varies from 0 (undamaged material) to 1 (fully damaged material). As either of these damage indices approach 1, the Biot coefficient drops to 0, and the effect of pore pressurization is eliminated at that material point.

Pore pressure was computed by the Simple Integrated Fission Gas Release and Swelling (SIFGRS) model [37] in Bison. This model computes the current pressure in gas bubbles, as well as the mechanical equilibrium pressure, which is the sum of the bubble surface tension and hydrostatic stress in the surrounding medium. The pressure applied in computing the effective stress (Equation 4.15) is the overpressure, which is the difference between the current pressure and equilibrium pressure. It is important to note that this pore pressure model is not intended for use in regions of the fuel with HBS, but is being used as a placeholder for proof-of-concept simulations. When a model that works in both non-HBS and HBS regions becomes available such a model should be used in its place.

The smeared cracking model used here is based on the approach of Rashid [38], which represents the fuel as an orthotropic material upon initiation of the first crack, which occurs when the first principal stress exceeds the material strength. The orientation of the crack is fixed, and additional cracks can form if the tensile stress in a direction orthogonal to the first crack direction exceeds the tensile strength. An exponential softening law is used for cracks that form in the plane of a Cartesian model, while a power-law model is used for out-of-plane cracks in lower-dimensional models, based on the findings in [39].

Figure 4.4 shows representative simulation results from the prior study for Studsvik Rod 191 at the end of the simulated LOCA transient. Contours of the predicted extent of in-plane damage are shown for a case that included the effects of pore pressurization, and one that did not. These results clearly indicate more extensive damage around the perimeter of the pellet in the case that included pore pressurization than in the case that excluded that effect. That should be expected because pore pressurization would result in tensile stresses around the perimeter of the pellet in the region where there is significant overpressurization. A less intuitive outcome from this model is that there is more extensive cracking in the center of the pellet in the case without pore pressurization. Because the pore pressure is relatively low in the center of the pellet, it would intuitively have little effect in the region in the center of the pellet.

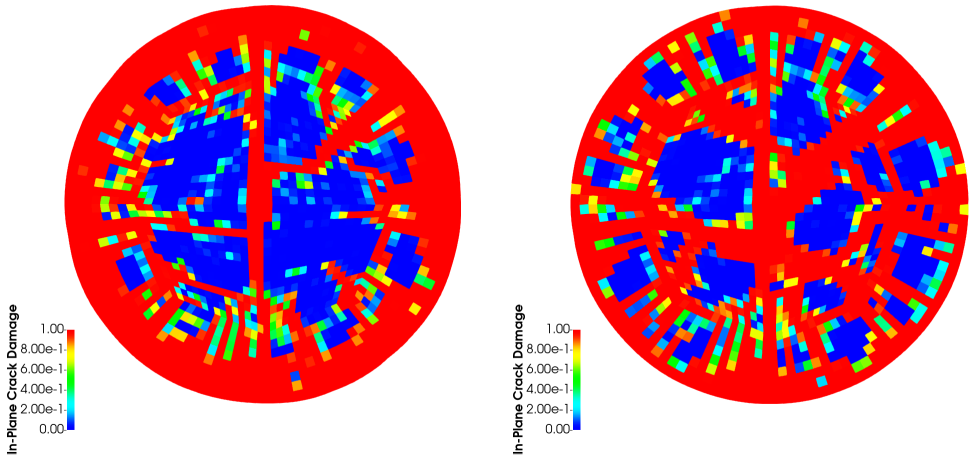

(a) (b)

Figure 4.4. Smeared-cracking-model-predicted in-plane damage in fuel at the end of a LOCA transient, as reported in [34], showing results (a) including pore-pressure effects and (b) excluding pore-pressure effects.

4.3.2 Updated simulations of pore-pressurization effects

In the present effort, further studies were performed on the smeared-cracking model of Studsvik Rod 191 that was discussed in the prior section. There were two objectives: (1) to better understand the causes of the counter-intuitive, more extensive cracking in the center of the pellet in the case excluding pore-pressure effects, and (2) to begin to incorporate the pulverization criterion based on mesoscale modeling developed in Section 4.2) in engineering-scale calculations.

One potential cause for the more extensive cracking in the center of the pellet is sensitivity of the cracking model to the size of the simulation time steps. Similar to most models that represent degradation of material strength, the smeared cracking model can make convergence of the nonlinear solutions difficult. Because of this, a common practice with this model, which is taken here, is to base the current solution on the degraded elastic response using the damage predicted in the previous step, and not update the stress in the current step for evolving damage. This approach results in an explicit integration of the damage model in an otherwise implicit solution.

Treating the damage in this way greatly improves the ability to obtain converged solutions, but makes the computed fracture patterns sensitive to the time step. If the chosen time steps are too large, the cracking model can predict damage spread out over an unrealistically large region. In the present effort, a scheme was used to control the time step to limit the damage increment in the model to minimize time-stepping-induced errors. The increment in the damage index for the first in-plane crack, averaged over the fuel domain, was limited to 0.005. The cracks tend to propagate rapidly during events such as power changes or transients, but propagate very little during steady-state conditions. This time-step limiting mechanism thus resulted in very small time steps being taken at some points in both the base irradiation and LOCA transients, but had no effect on the time steps during much of the base irradiation.

Figure 4.5 shows contours of the in-plane cracking predicted by the smeared cracking model of Studsvik Rod 191

with the updated model with the aforementioned time-step controls. Results are shown both at the beginning and end of the transient, which occurred after a long base irradiation. The specific locations of the cracks vary somewhat from the earlier results, but these models still indicate that when pore pressurization is considered, significantly more cracking occurs around the pellet periphery. More extensive cracking is still predicted in the center of the pellet in the case that excludes pore-pressurization effects, but the difference between the cases that include and exclude pore-pressurization is reduced somewhat from the earlier results.

The 2-D cross-section models employed here are somewhat limited in their ability to represent cracking because they average the behavior over the whole pellet height. The observed crack broadening in the center of the pellet is very likely an artifact of the 2-D modeling assumptions. 3-D models of this problem are being developed to determine whether this is the case.

The smeared-cracking models employed here don't explicitly distinguish between fracture and pulverization. The same tensile-stress criterion is used in both cases, but pulverization is driven by internally-generated stresses from bubble overpressurization rather than stresses generated externally to a given material point by phenomena such as thermal gradients. The fracture criterion is based on the original material strength, and does not account for HBS effects. Ideally, a criterion accounting for HBS effects such as that presented in Section 4.2 should be used to predict pulverization, and that criterion could be used to trigger loss of strength in a similar manner to the loss of strength due to the fracture criterion.

As a step toward this goal, the pulverization criterion of Equation 4.14 was evaluated at all material points in the smeared-cracking model to indicate the locations of regions with expected pulverization. This criterion was modified slightly for use with the poromechanics model, in that the external hydrostatic stress (P_{ext}) was reduced by the amount of the macroscopic applied pore-pressurization stress. This to account for the fact that applying a pore pressure in the poromechanics model on an unrestrained body results in a macroscopic tensile stress, which would be consistent with applying an external hydrostatic stress to the phase-field models that the pulverization criterion is based on. Since the stresses due to pore pressurization are explicitly applied to the pore in the phase-field model, it would not be appropriate to apply an additional stress.

This simulation does not yet take advantage of the updated evolution equation for bubble pressure in the HBS region developed in Section 4.1. Rather, it employs the prior approach based on an ideal gas law with assumptions of initial temperature and pressure described at the beginning of that Section. Additional development is needed to provide a pore pressure model that smoothly transitions from non-HBS to HBS behavior, and which can be used both to account for the effects of overpressurization on the mechanical response and within a criterion for pulverization.

Figure 4.6 shows contours of the pulverization indicator when run on the smeared-cracking model. The indicator goes from 0 for material that has not pulverized to 1 for pulverized material. This indicator only has discrete values of 0 or 1 at a given quadrature point, but the values shown here are averaged over the quadrature points in an element, so they have values between 0 and 1. Results are shown at the beginning and end of the LOCA transient. A small amount of pulverization is indicated around the outer rim before the transient, and as would be expected, that pulverization region increases in width during the transient due to the increase in pore pressure. It is important to note that the pulverization region is much narrower than the region with increased damage predicted by the smeared-cracking model with pore pressurization. Different criteria were used for failure in these methods, and different assumptions were made for the

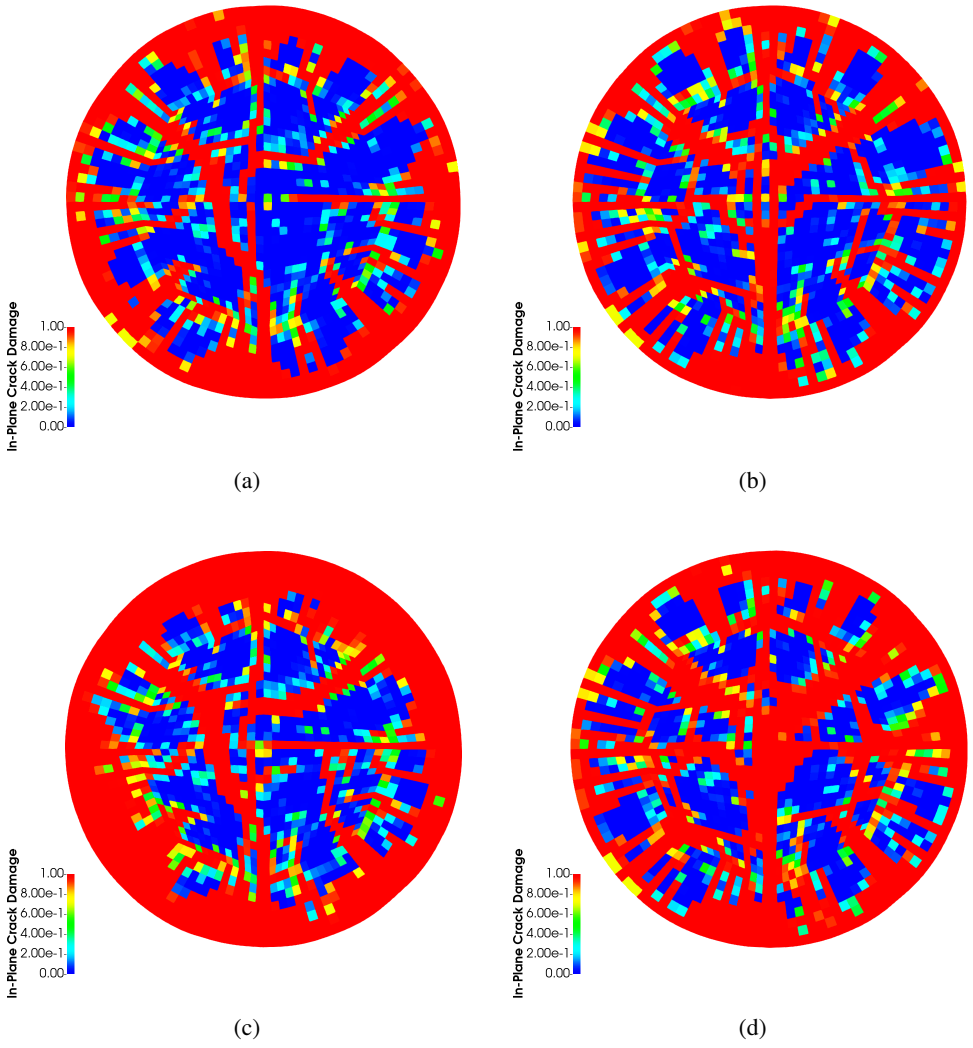

Figure 4.5. Updated smeared-cracking-model-predicted in-plane damage in fuel at the beginning and end of a LOCA transient. Results are shown (a) at the beginning of the transient including pore-pressure effects, (b) at the beginning of the transient excluding pore-pressure effects, (c) at the end of the transient including pore-pressure effects, and (d) at the end of the transient excluding pore-pressure effects.

pore pressures used. Future efforts to use a consistent pore pressure model for HBS and non-HBS regions will address that.

The only source of azimuthal variations in the predicted pulverization would be local stresses, and some effects of local stress variations can be seen. The regions with more pulverization appear to correspond with the regions of major radial cracks. Similarly, the case that includes the effects of pore pressurization, and which predicts more damage around the fuel perimeter, shows slightly more pulverization than the case that excludes that effect.

Some additional developments are needed to fully incorporate the pulverization criterion into the smeared cracking model. These include incorporating a unified pore pressurization model that operates in HBS and non-HBS regions, and consistently using that pore pressure both to affect the mechanical response and to predict pulverization. In addition, the strength loss due to pulverization still needs to be handled in a consistent manner and in a way that can be used in conjunction with the model for externally-driven fracture.

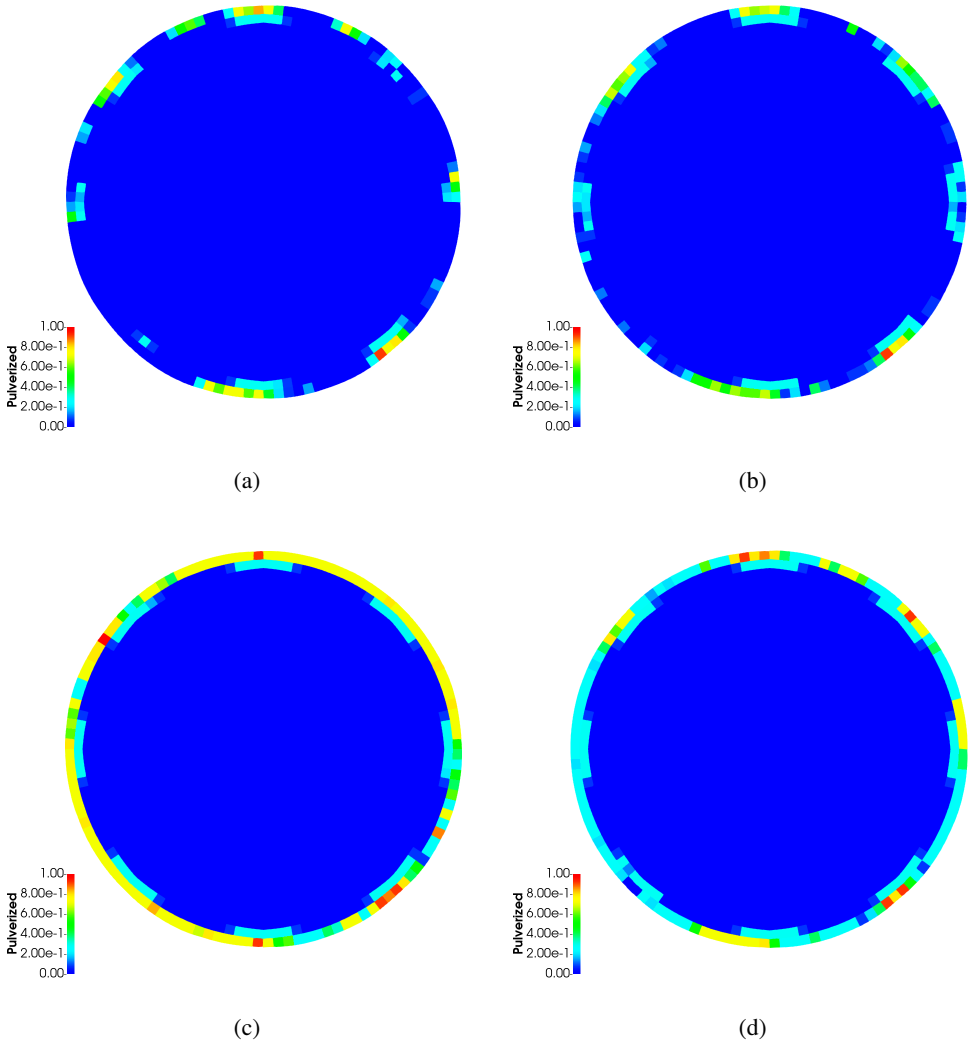

Figure 4.6. Pulverization indicator damage in fuel at the beginning and end of a LOCA transient. Results are shown (a) at the beginning of the transient including pore-pressure effects, (b) at the beginning of the transient excluding pore-pressure effects, (c) at the end of the transient including pore-pressure effects, and (d) at the end of the transient excluding pore-pressure effects.

5. TRANSIENT FISSION GAS RELEASE DURING PULVERIZATION

5.1 Context regarding transient fission gas release

Understanding the behavior of the fuel from the HBS region is paramount to extend the burnup usage for the existing nuclear fleet. One of the main challenges is to accurately predict fission gas release (FGR) from high-burnup fuel, especially outside of normal conditions (e.g., Reactivity Insertion Accident (RIA) and LOCA conditions). Although FGR during normal conditions for non-HBS fuel is fairly well understood [37, 40, 41], several experimental programs exhibited a large increase in FGR during transients [42, 43, 44, 45]. This contribution, called transient FGR (tFGR), becomes increasingly significant with increasing burnup and may impact the ballooning and burst behavior of high-burnup fuel [5, 6]. These experimental programs also concluded that tFGR originates from inter-granular bubbles, and tFGR is a result of (1) bubble interconnection and (2) fuel pulverization, which lead to the release of the gas located in over-pressurized bubbles.

Despite these insights, the mechanisms governing tFGR remain unclear. It is a complex phenomenon that depends on many variables (e.g., burnup, irradiation history, temperature history, fuel fragmentation, hydrostatic pressure), and for which only a limited amount of experimental data is yet available. In this study, we focus on the potential contribution of pulverization of the outer rim of the fuel pellets on tFGR, which is estimated to correspond to 32-45% of fission gas [44, 45, 46]. We thus neglect other contributions (e.g., release from the central zone of the pellet, which is estimated to represent 22% of the fission gas [44, 45, 46]). The proposed mechanism relies on the sudden opening of many pores during fuel fragmentation, thus releasing their fission gas. We therefore leverage the model of bubble growth introduced in Section 2 and the pulverization criteria developed in Section 4 to predict the amount of FGR attributable to pulverization, in the hope of accounting for a significant portion of tFGR.

The link between pore microstructure and FGR during pulverization is detailed in Section 5.2. We describe the mechanism for tFGR during pulverization, as explored in this study, and the description of FGR was quantified based on bubble size/pressure, fragment size, and porosity. This quantification provides a function usable at the engineering scale to determine tFGR during pulverization. Section 5.3 concludes this part of the report and provide insights for future work.

5.2 tFGR during pulverization: a pore-structure-dependent mechanism

5.2.1 First approximation: all fission gas is released during pulverization

A coarse, conservative approximation of the amount of FGR during pulverization could consider that all the FG contained in the pulverized fuel, n_{FG}^{pul}, is released. This amount would be equal to

$$n_{FG}^{pul} = \frac{V_b^{pul} P_{FG}}{RT}, \tag{5.1}$$

where V_b^{pul} is the bubble volume in pulverized fuel, P_{FG} is the bubble pressure, R is the gas constant, and T is the temperature. V_b^{pul} is defined as

$$V_b^{pul} = pV^{pul}, \tag{5.2}$$

where p is the fuel porosity, as provided by the model in Section 2, and V^{pul} is the volume of pulverized fuel, as provided by the model in Section 4. P_{FG} is provided by the model in Section 2.

This conservative assumption more than likely significantly overestimates the amount of tFGR during pulverization. To provide a more realistic estimation of tFGR, we refine this assumption for the rest of this study to account for fragment size, bubble size, and porosity in order to estimate the fraction of pores exposed during pulverization.

5.2.2 Refinement: only open pores release fission gas

During fuel pulverization, only a fraction of the pores become exposed to free surfaces and release fission gas. The amount of FGR due to pulverization, rather than being defined by Eq. (5.1), is actually equal to

$$n_{FG}^{pul} = \frac{V_{b,open}^{pul} P_{FG}}{RT} = f_V^{pul} \frac{V_b^{pul} P_{FG}}{RT}, \tag{5.3}$$

where $V_{b,open}^{pul}$ is the volume of pores that become exposed during fragmentation, and

$$f_V^{pul} = \frac{V_{b,open}^{pul}}{V_b^{pul}} = \frac{\sum_{bi} V_{bi,open}^{pul}}{\sum_{bi} V_{bi}^{pul}} \tag{5.4}$$

is the volume fraction of pores opened during fuel pulverization, with *bi* designating each pore. These definitions are illustrated in Fig. 5.1. f_V^{pul} is expected to depend on pore structure, fragment size, and porosity, and this dependence has to be quantified.

5.2.3 Pore structure generation and characterization

To quantify how f_V^{pul} - and by extension n_{FG}^{pul} - depends on fragment size, pore size, and porosity, a Python script was written to automatically generate 3-D pore structures and determine the corresponding f_V^{pul}. Given a specific fragment size, bubble size, and porosity, the algorithm adds pores with the desired radius at random locations in and around

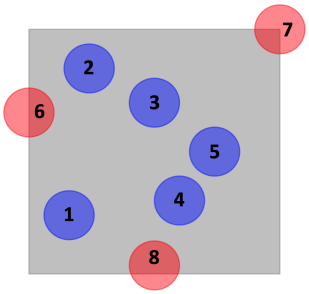

Figure 5.1. 2-D illustration of the definition of $V_{b,open}^{pul}$ and f_V^{pul}, and their importance in determining FGR during pulverization. The fragment is shown in light grey, and the bubbles are shown in blue and red, along with number labels. All the bubbles in this microstructure are assumed to have the same radius R. Bubbles 1 through 5 (blue) are completely contained in the fragment, and thus do not contribute to FGR. Their contribution to the total bubble volume is equal to $5 \times 4/3\pi R^3$. Their contribution to the open bubble volume is 0. However, bubbles 6, 7, and 8 became exposed during pulverization. Their contribution to the total bubble volume is equal to $1/2 \times 4/3\pi R^3$, $1/4 \times 4/3\pi R^3$, and $3/4 \times 4/3\pi R^3$, respectively, as is their contribution to the open bubble volume. For this pore structure: $V_b^{pul} = 13/2 \times 4/3\pi R^3$, $V_{b,open}^{pul} = 3/2 \times 4/3\pi R^3$, and $f_V^{pul} = 3/13 = 0.231$.

a cube fragment until the desired porosity is reached. Each time a pore is added to the fragment, its contributions to the total pore volume V_{bi}^{pul} and open pore volume $V_{bi,open}^{pul}$ are calculated. When the pore structure is created, its f_V^{pul} is derived. Note that two pores cannot be in contact with each other, and that even though bubbles can be partly outside the fragment, porosity calculations only include the pore volume that intersects with the fragment. Examples of generated pore structures at different porosity levels and different bubble sizes are shown in Fig. 5.2.

5.2.4 Predicting tFGR as a function of pore structure, fragment size, and porosity

To ensure the usefulness and applicability of this study, we used relevant porosity levels and pore/fragment sizes for HBS. The porosity levels therefore varied between 1 and 13% [49, 50, 31]. Concerning fragment and bubble sizes, preliminary results revealed that f_V^{pul} depends mostly on the ratio (r_b/l_f) of bubble radius r_b to fragment size l_f, and not on each of these lengths separately. This is due to the fact that f_V^{pul} depends on the probability of a given pore to be in contact with a fragment surface, which depends on r_b/l_f. As a result, the bubble and fragment sizes were normalized so that r_b/l_f was defined somewhere between 0.01 and 0.1. These values are relevant for fragment sizes of tens of microns [47, 48] and bubble radii between 0.01 μm and 5 μm [51, 47, 48, 52, 46].

Different pore structures with relevant characteristics are therefore generated using the Python script, as described in Section 5.2.3. For each porosity and bubble radius-to-fragment-size ratio, 100 pore structures are generated so that the potential statistical variations in f_V^{pul} can be shown. The results are provided in Fig. 5.3. The data generated by the Python script can be fitted using a linear regression, resulting in

$$f_V^{pul} = c_p p + c_r \frac{r_b}{l_f} + c_0, \tag{5.5}$$

with $c_p = 0.03$ (-) the coefficient for the porosity, $c_r = 5.17$ (-) the coefficient for the bubble-radius-to-fragment-size

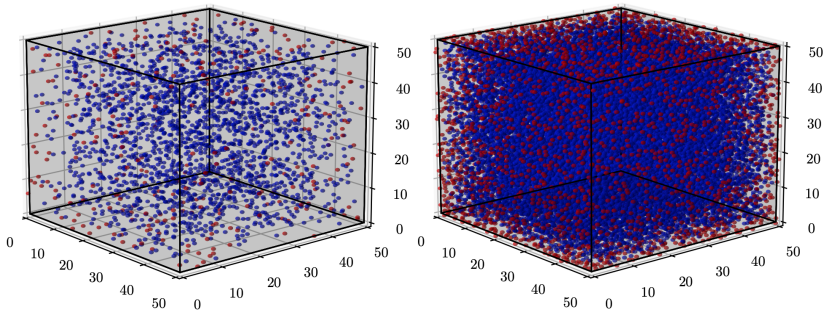

(a) $p = 1\%$, $r_b = 0.5$: $f_V^{pul} = 0.066$

(b) $p = 10\%$, $r_b = 0.5$: $f_V^{pul} = 0.128$

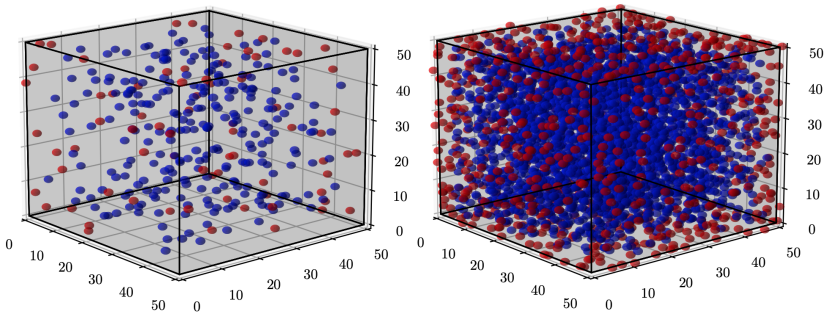

(c) $p = 1\%$, $r_b = 1$: $f_V^{pul} = 0.061$

(d) $p = 10\%$, $r_b = 1$: $f_V^{pul} = 0.122$

Figure 5.2. Example of generated pore structures at different porosity levels p and bubble radii r_b, with the fragment size fixed at $l_f = 50$ μm [47, 48]. Pores completely contained in the fragment are shown in blue, whereas pores opened during pulverization (i.e., in contact with the fragment surface) are shown in red. For each pore structure, f_V^{pul} is provided. Note that due to the random nature of the algorithm, different f_V^{pul} can be obtained for the given porosity and bubble radius values.

ratio, and $c_0 = 0.02$ (-) the constant. f_V^{pul} does not vary significantly with porosity, but increases on average with r_b/l_f. Note that c_0 is, as expected, close to 0. The amount of tFGR due to pulverization should indeed tend toward 0 when the porosity decreases. It is important to note that although the fit follows the average trend of f_V^{pul} quite successfully, the quality of the fit is as low as $R^2 = 0.79$. This is due to the fact that, for some pore structures, the random nature of the pore placement leads to large variations in f_V^{pul} values. This is especially true for lower porosities and large r_b/l_f values (see Figs. 5.3b and 5.3c), since the position of a few large bubbles significantly affects f_V^{pul}.

5.3 Conclusions and future work

The current study investigates the amount of tFGR due to fuel pulverization using a mechanistic model based on the fraction of pores exposed during fragmentation. Using randomly generated pore structures relevant to the HBS region of UO_2 fuel, we determined the fraction of FG that is susceptible to release during pulverization. This fraction of

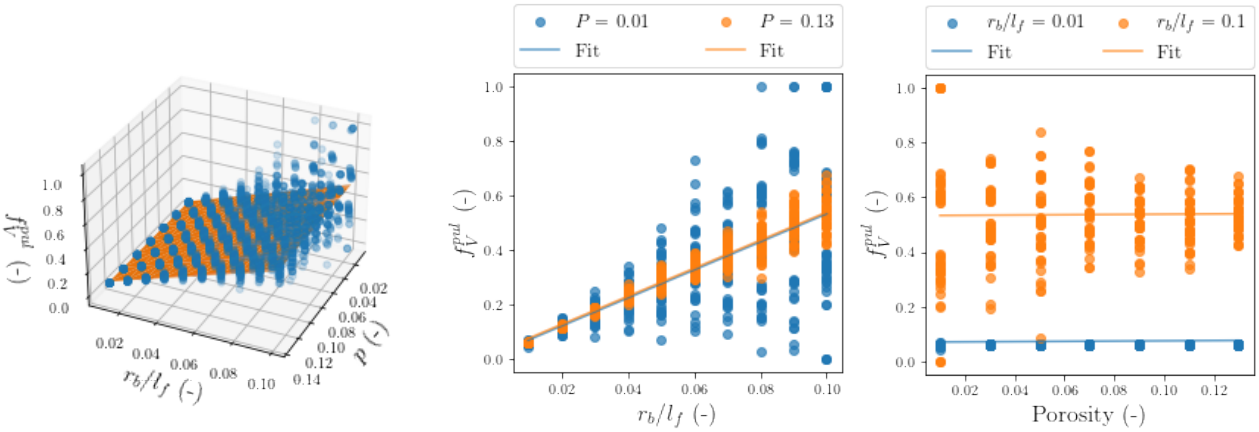

(a) (b) (c)

Figure 5.3. Predicted f_V^{pul} values for different pore structures in fuel fragments, along with a fit using a linear regression. (a) Shows the data in 3-D. (b, c) Show the data along r_b/l_f for extreme porosity values, and along the porosity for extreme r_b/l_f values, respectively. f_V^{pul} does not significantly depend on porosity, but increases on average with r_b/l_f. Despite an appropriate fitting, the quality of the fit is equal to $R^2 = 0.79$, due to large variations in f_V^{pul} for some pore structures, especially for low porosities.

FG that contributes to tFGR is modeled as a function of porosity and the bubble-size-to-fragment-size ratio (r_b/l_f). Although it does not significantly depend on fuel porosity, tFGR increases with r_b/l_f. It is also important to note that the uncertainty of the model increases for large r_b/l_f values and low porosity values.

This effort represents a first step toward modeling and quantifying tFGR caused by pulverization. The current model still needs to be validated by being implemented in BISON and comparing the predictions against experimental measurements, which will be the focus of future work. Moreover, several important aspects were left unexplored in this study. For example, the effect of bubble size distribution was not quantified. Furthermore, using a Gaussian process rather than a linear regression to fit the fraction of FG released during pulverization would provide a valuable quantification of the variance and uncertainty involved.

Once the tFGR contribution from pulverization is well understood and quantified, it would be interesting to compare the prediction from the current work against those from other models, such as the one published in Ref. [53]. Future work will also investigate other mechanisms that contribute to tFGR. In particular, the current work neglects FGR from the center of the pellet, which has been shown to release 22% of it initial inventory [46]. Accounting for FGR from the center of the pellet might be necessary in accounting for the total tFGR.

6. OVERALL CONCLUSIONS AND FUTURE WORK

In this report, lower length scale activities to inform the Bison model of pulverization of high burnup UO_2 fuel were described. In Section 1, the motivation for the work and a general description of the strategy were given.

In Section 2, the grand-potential based phase field model for fission gas bubble evolution was extended to include interstitials, and to consider the effect of mobile multi-vacancy clusters that accompany Xe atoms. It was shown that two different simplified models with vacancies only could match the growth rate of the full vacancy-interstitial model: a model that included an effective sink for vacancies, and a model with a parameterized vacancy source term only. However, these models were only tested on bubbles in chemical equilibrium with the matrix phase; future work should consider the effect of mechanical equilibrium as well. Using the parameterized source term approach, growth of bubbles in the HBS region was simulated using a coupled phase-field/cluster dynamics approach. Using this approach prevented spurious formation of intragranular bubbles as had been seen in previous simulations of HBS bubble growth. When the diffusion coefficients of grain boundaries and surfaces were accounted for, depletion of Xe in grain interiors and enhanced growth of bubbles was observed, consistent with experimental observations. Bubble pressures determined from these simulations were somewhat lower than the dislocation punching pressure, in contrast to previous phase-field simulations that showed some pressures above and some below dislocation punching pressure for different bubble sizes. However, the phase-field model does not yet account for surface tension effects, so for the present time, the initial bubble pressure in the HBS region in the Bison model will continue to be set based on the dislocation punching pressure.

In Section 3, a phase-field fracture model was used to simulate pulverization surrounding bubbles in the HBS region. 3-D phase-field fracture simulations were performed, in contrast to previous work that used 2-D simulations to determine the pulverization criterion. Model simplifications to reduce the computational cost of the 3-D simulations were implemented based on 2-D testing, including not resolving the grain structure and using a larger element size. The critical pressure for pulverization was determined for varying porosity, external pressure, and grain boundary fracture strength.

Section 4 focused on improvements to the Bison pulverization model based on the lower length scale simulations. An evolution equation for bubble pressure and radius was added to the Bison model to account for gas and vacancy flux. Bubbles are overpressurized at the time of HBS formation, leading to a decrease in pressure and increase in radius. Based on the phase-field fracture results, a new function for critical bubble pressure was fit for Bison. The effects of these modifications on existing Bison assessments of LOCA transients and pulverization will be completed in a forthcoming engineering-scale milestone. A poromechanics-based approach was used to include the effect of

bubble overpressurization on the overall stress state in the material in pre-HBS microstructures. A new time stepping approach was used that reduced differences between cases that include and exclude pore pressurization. Including pore pressurization effect on local stress calculations results in increased pulverization.

In Section 5, to inform a future model of tFGR resulting from pulverization, fragments with varying porosities and average bubble sizes were simulated. The fraction of gas released was primarily dependent on the ratio of bubble size to fragment size and porosity. A linear function for the fraction of gas released was fit to this data; however, the quality of the fit was relatively low. In future work, the data will be fit with a Gaussian process approach instead of linear regression.

Bibliography

[1] V. V. Rondinella and T. Wiss. "The high burn-up structure in nuclear fuel". In: *Materials Today* 13 (2010), pp. 24–32.

[2] N. Capps et al. "A Critical Review of High Burnup Fuel Fragmentation, Relocation, and Dispersal under Loss-Of-Coolant Accident Conditions". In: *Journal of Nuclear Materials* 546 (2021), p. 152750. DOI: https://doi.org/10.1016/j.jnucmat.2020.152750.

[3] Z. Xiao et al. "A quantitative phase-field model of gas bubble evolution in UO_2". In: *Computational Materials Science* 184 (2020), p. 109867.

[4] C.A. Smith et al. "Investigation of high burnup structure in U-Mo fuels". In: *Journal of Nuclear Materials* 563 (2022).

[5] U.S. Nuclear Regulatory Commission (NRC). *RIL 2021-13, Interpretation of Research on Fuel Fragmentation, Relocation, and Dispersal at High Burnup*. (ADAMS Proprietary Accession No. ML21313A110), 2021.

[6] G. Khvostov. "Analytical criteria for fuel fragmentation and burst FGR during a LOCA". In: *Nuclear Engineering and Technology* 52 (10 Oct. 2020), pp. 2402–2409. ISSN: 1738-5733. DOI: 10.1016/J.NET.2020.03.009.

[7] L. K. Aagesen et al. *Mesoscale simulations to inform microstructure- based pulverization criterion in high-burnup UO_2*. Tech. rep. INL/EXT-21-64275. Idaho National Laboratory, 2021.

[8] L. K. Aagesen et al. "Phase-field modeling of fission gas bubble growth on grain boundaries and triple junctions in UO_2 nuclear fuel". In: *Computational Materials Science* 161 (2019), pp. 35–45. ISSN: 0927-0256. URL: <GotoISI>://WOS:000462165100005.

[9] C Matthews et al. "Cluster dynamics simulation of xenon diffusion during irradiation in UO_2". In: *Journal of Nuclear Materials* in press (2020), p. 152326.

[10] L. K. Aagesen et al. "Grand-potential-based phase-field model for multiple phases, grains, and chemical components". In: *Physical Review E* 98 (2018), p. 023309.

[11] Dong-Uk Kim et al. "Modeling mesoscale fission gas behavior in UO2 by directly coupling the phase field method to spatially resolved cluster dynamics". In: *Materials Theory* 6.7 (2022).

[12] M. Plapp. "Unified derivation of phase-field models for alloy solidification from a grand-potential functional". In: *Physical Review E* 84.3 (2011), p. 031601. ISSN: 1539-3755. URL: <GotoISI>://WOS:000294569000002.

[13] Ian Greenquist et al. “Development of a microstructural grand potential-based sintering model”. In: *Computational Materials Science* 172 (2020). DOI: https://doi.org/10.1016/j.commatsci.2019.109288.

[14] Ian Greenquist et al. “Grand potential sintering simulations of doped UO2 accident-tolerant fuel concepts”. In: *Journal of Nuclear Materials* 532 (2020). DOI: https://doi.org/10.1016/j.jnucmat.2020.152052.

[15] Larry K. Aagesen et al. “Phase-field simulations of intergranular fission gas bubble behavior in U3Si2 nuclear fuel”. In: *Journal of Nuclear Materials* 541 (2020). DOI: https://doi.org/10.1016/j.jnucmat.2020.152415.

[16] N. Moelans, B. Blanpain, and P. Wollants. “Quantitative analysis of grain boundary properties in a generalized phase field model for grain growth in anisotropic systems”. In: *Phys. Rev. B* 78 (2008), p. 024113.

[17] JB Ainscough, BW Oldfield, and JO Ware. “Isothermal grain growth kinetics in sintered UO_2 pellets”. In: *Journal of Nuclear Materials* 49.2 (1973), pp. 117–128.

[18] M. Idiri et al. “Behavior of actinide dioxides under pressure: UO_2 and ThO_2”. In: *Physical Review B* 70.1 (2004). ISSN: 1098-0121. URL: <GotoISI>://WOS:000222996300040.

[19] J. B. Wachtman et al. “Elastic Constants of Single Crystal UO_2 at 25 Degrees C”. In: *Journal of Nuclear Materials* 16.1 (1965), pp. 39–41. ISSN: 0022-3115. URL: <GotoISI>://WOS:A19657630000005.

[20] D.A. Knoll and D.E. Keyes. “Jacobian-free Newton-Krylov methods: a survey of approaches and applications”. In: *J. Comput. Phys.* 193 (2004), pp. 357–397. URL: https://www.sciencedirect.com/science/article/pii/S0021999103004340.

[21] Benjamin S. Kirk et al. “libMesh: a C++ library for parallel adaptive mesh refinement/coarsening simulations”. In: *Engineering with Computers* 22 (2006), pp. 237–254. ISSN: 09270256. DOI: 0.1007/s00366-006-0049-3.

[22] R. Perriot et al. “Atomistic modeling of out-of-pile xenon diffusion by vacancy clusters in UO_2”. In: *Journal of Nuclear Materials* 520 (2019), pp. 96–109.

[23] Olander et al. “On the role of grain boundary diffusion in fssion gas release”. In: *Journal of Nuclear Materials* 6.7 (2001).

[24] J. A. Turnbull et al. “The diffusion coefficients of gaseous and volatile species during the irradiation of uranium dioxide”. In: *Journal of Nuclear Materials* 107 (1982), pp. 168–184. URL: https://www.sciencedirect.com/science/article/pii/0022311582904196.

[25] Hj Matzke. “Atomic Transport Properties in U02and Mixed Oxides (u,pU)O2”. In: *J. Checm Soc.* 83 (1987), pp. 1121–1142.

[26] L Aagesen et al. *Determine Fragmentation Criteria in High-burnup UO_2 Fuel during Accident Conditions*. Tech. rep. INL/EXT-20 0- Rev. 0. Idaho National Lab.(INL), Idaho Falls, ID (United States), 2020.

[27] White et al. “A new fission-gas release model”. In: *Journal of Nuclear Materials* 6.7 (1983).

[28] Sudipta Biswas, Daniel Schwen, and Jason D. Hales. “Development of a finite element based strain periodicity implementation method”. In: *Finite Elements in Analysis and Design* 179 (2020). DOI: https://doi.org/10.1016/j.finel.2020.103436.

[29] K. Nogita and K. Une. "Irradiation-induced recrystallization in high burnup UO_2 fuel". In: *Journal of Nuclear Materials* 226.3 (1995), pp. 302–310. DOI: 10.1016/0022-3115(95)00123-9.

[30] K. Kulacsy. "Mechanistic model for the fragmentation of the high-burnup structure during LOCA". In: *Journal of Nuclear Materials* 466 (2015), pp. 409–416.

[31] Tommaso Barani et al. "Modeling high burnup structure in oxide fuels for application to fuel performance codes. Part II: Porosity evolution". In: *Journal of Nuclear Materials* 563 (May 2022), p. 153627. ISSN: 0022-3115. DOI: 10.1016/J.JNUCMAT.2022.153627.

[32] D.R.Olander. *Fundamental aspects of nuclear reactor fuel elements*. Technical Information Center, Office of Public Affairs Energy Research and Development Administration, 1976.

[33] T. Kogai. "Modelling of fission gas release and gaseous swelling of light water reactor fuels". In: *Journal of Nuclear Materials* 244 (1997), pp. 131–140.

[34] Benjamin W. Spencer and Kyle A. Gamble. *Engineering Scale Modeling of Local Fuel Stress States Due to Pore Pressure and Confining Effects*. Tech. rep. XXXX. Idaho National Laboratory, In Review.

[35] Maurice A. Biot. "General Theory of Three-Dimensional Consolidation". en. In: *Journal of Applied Physics* 12.2 (Feb. 1941), pp. 155–164. DOI: 10.1063/1.1712886. URL: http://aip.scitation.org/doi/10.1063/1.1712886 (visited on 12/08/2020).

[36] Maurice A Biot and DG Willis. "The elastic coefficients of the theory of consolidation". In: *J. appl. Mech* 24 (1957), pp. 594–601.

[37] Giovanni Pastore et al. "Physics-based modelling of fission gas swelling and release in UO2 applied to integral fuel rod analysis". In: *Nuclear Engineering and Design* 256 (Mar. 2013), pp. 75–86. ISSN: 0029-5493. DOI: 10.1016/J.NUCENGDES.2012.12.002.

[38] Y.R. Rashid. "Mathematical modeling and analysis of fuel rods". en. In: *Nuclear Engineering and Design* 29.1 (Nov. 1974), pp. 22–32. ISSN: 00295493. DOI: 10.1016/0029-5493(74)90095-8. (Visited on 03/09/2018).

[39] Benjamin W. Spencer and Russell J. Gardner. *Improved LWR Fuel Rod Mechanics Models*. Tech. rep. INL/EXT-18-44749. Idaho National Laboratory, 2018. DOI: 10.2172/1467423.

[40] G Pastore et al. "Modeling Fission Gas Behaviour with the BISON Fuel Performance Code". In: (2017). URL: http://www.inl.gov.

[41] G. Pastore et al. "An effective numerical algorithm for intra-granular fission gas release during non-equilibrium trapping and resolution". In: *Journal of Nuclear Materials* 509 (Oct. 2018), pp. 687–699. ISSN: 0022-3115. DOI: 10.1016/J.JNUCMAT.2018.07.030.

[42] W. Wiesenack. *HPR-383, Summary and Comparison of LOCA Tests with BWR Fuel in the Halden Reator Project Test Series IFA-650*. Halden Reactor Project, 2015.

[43] et al. Magnusson P. *STUDSVIK/N-19/105 STUDSVIK-SCIP III-253—Subtask 1.1: Fuel fragmentation, relocation and dispersal, Final Summary Report*. Studsvik Nuclear AB, 2020.

[44] Y. Pontillon et al. *Fission gas release under fast transient and LOCA conditions: Analytical devices implemented at Commissariat a l'Energie Atomique (IAEA-TECDOC–1320)*. International Atomic Energy Agency (IAEA), 2002. URL: https://inis.iaea.org/search/search.aspx?orig_q=RN:34010869.

[45] Yves Pontillon et al. "Experimental and theoretical investigation of fission gas release from UO2 up to 70 GWd/t under simulated LOCA type conditions: The GASPARD program". In: *Proceedings of the 2004 International Meeting on LWR Fuel Performance* (June 2004), pp. 490–499.

[46] M. Marcet et al. "High Burn up Structure Contribution to the Fission Gas Release under Transient Conditions". In: Sept. 2009, p. 268.

[47] Katsumi Une, Shinji Kashibe, and Akira Takagi. "Fission Gas Release Behavior from High Burnup UO2 Fuels under Rapid Heating Conditions". In: *https://doi.org/10.1080/18811248.2006.9711208* 43 (9 2006), pp. 1161–1171. ISSN: 00223131. DOI: 10.1080/18811248.2006.9711208. URL: https://www.tandfonline.com/doi/abs/10.1080/18811248.2006.9711208.

[48] J. P. Hiernaut et al. "Fission product release and microstructure changes during laboratory annealing of a very high burn-up fuel specimen". In: *Journal of Nuclear Materials* 377 (2 July 2008), pp. 313–324. ISSN: 0022-3115. DOI: 10.1016/J.JNUCMAT.2008.03.006.

[49] J. Spino et al. "Stereological evolution of the rim structure in PWR-fuels at prolonged irradiation: Dependencies with burn-up and temperature". In: *Journal of Nuclear Materials* 354 (1-3 Aug. 2006), pp. 66–84. ISSN: 0022-3115. DOI: 10.1016/J.JNUCMAT.2006.02.095.

[50] F. Cappia et al. "Critical assessment of the pore size distribution in the rim region of high burnup UO2 fuels". In: *Journal of Nuclear Materials* 480 (Nov. 2016), pp. 138–149. ISSN: 0022-3115. DOI: 10.1016/J.JNUCMAT.2016.08.010.

[51] Katsumi Une, Shinji Kashibe, and Kimio Hayashi. "Fission Gas Release Behavior in High Burnup UO2 Fuels with Developed Rim Structure". In: *https://doi.org/10.1080/00223131.2002.10875557* 39 (2002), pp. 668–674. ISSN: 00223131. DOI: 10.1080/00223131.2002.10875557. URL: https://www.tandfonline.com/doi/abs/10.1080/00223131.2002.10875557.

[52] M. Marcet et al. "In situ Characterization of UO2 Microstructure Changes During an Annealing Test in an Environmental Scanning Electron Microscope". In: *MRS Online Proceedings Library (OPL)* 1215 (2009), pp. 157–162. ISSN: 0272-9172. DOI: 10.1557/PROC-1215-V16-44. URL: https://www.cambridge.org/core/journals/mrs-online-proceedings-library-archive/article/abs/in-situ-characterization-of-uo2-microstructure-changes-during-an-annealing-test-in-an-environmental-scanning-electron-microscope/A13516F89AE0A076C6D9E2721040ABAD.

[53] Lars O. Jernkvist. "Modelling of fine fragmentation and fission gas release of UO2 fuel in accident conditions". In: *EPJ Nuclear Sciences Technologies* 5 (2019), p. 11. ISSN: 2491-9292. DOI: 10.1051/EPJN/2019030. URL: https://www.epj-n.org/articles/epjn/full_html/2019/01/epjn190024/epjn190024.htmlhttps://www.epj-n.org/articles/epjn/abs/2019/01/epjn190024/epjn190024.html.